

INTERACTION OF MICROWAVE
FILAMENTS AND A BLUNT BODY
IN SUPERSONIC FLOW

BY FARNAZ FARZAN

A thesis submitted to the
Graduate School—New Brunswick
Rutgers, The State University of New Jersey
in partial fulfillment of the requirements
for the degree of
Master of Science
Graduate Program in Mechanical and Aerospace Engineering

Written under the direction of
Doyle D. Knight
and approved by

New Brunswick, New Jersey
OCTOBER, 2008

© 2008

FARNAZ FARZAN

ALL RIGHTS RESERVED

ABSTRACT OF THE THESIS

INTERACTION OF MICROWAVE FILAMENTS AND A BLUNT BODY IN SUPERSONIC FLOW

by FARNAZ FARZAN

Thesis Director: Doyle D. Knight

Recent experiments have demonstrated the capability of pulsed microwave energy deposition for drag reduction in supersonic flows. The principal mechanism of this phenomenon is the interaction of the hot filaments generated by the microwave energy pulse with the shock system formed by the aerodynamic body. In this work, the filament is modeled as a thin fluid region of high temperature. The interaction of the filament(s) with a cylindrical body at Mach number 1.89 is examined using the unsteady Euler equations. Two filament structures are considered, namely, 1) an infinitely long filament, and 2) a periodic train of finite filaments (at different frequencies). The development of the flow structure during the interaction is investigated. Furthermore, the drag reduction effectiveness and efficiency of the process of the interaction of the microwave filament(s) with the cylindrical shock layer for each case are studied.

Keywords: blunt body, stand-off distance, bow shock, recompression shock, expansion fan, microwave filament, contact discontinuity, Richtmeyer–Meshkov instability, lensing effect, vortex region, recirculation area, drag reduction, CFD

Dedication

To my family

Table of Contents

Abstract	ii
Dedication	iii
List of Tables	vii
List of Figures	viii
1. Introduction	1
1.1. Motivation	1
1.2. Literature Survey	2
1.2.1. Historical Overview	2
1.2.2. Experimental Articles	6
Kolesnichenko <i>et al</i> 2001	6
Lashkov <i>et al</i> 2003, 2004	7
Mashek <i>et al</i> 2004	7
Brovkin <i>et al</i> 2006	9
1.2.3. Numerical Articles	9
Kolesnichenko <i>et al</i> 2002	9
Kolesnichenko <i>et al</i> 2003	11
Azarova <i>et al</i> 2005	12
Lashkov <i>et al</i> 2006	12
Zheltovodov <i>et al</i> 2007	13
1.3. Statement of Objectives	14
1.3.1. Outline of the Thesis	15

2. Problem Statement	16
2.1. Problem Definition	16
2.2. Dimensionless Parameters	17
2.3. Parameters Investigated	17
3. Methodology	19
3.1. Governing Equations	19
3.1.1. Nondimensionalization	20
3.1.2. Governing Equations in Dimensionless Form	21
3.1.3. Boundary Conditions in Dimensionless Form	22
3.1.4. The Integral Form of the Conservation Laws	23
3.2. Numerical Algorithm	23
3.2.1. Flux Vector Splitting Method	25
Van Leer's Method	26
3.2.2. Reconstruction Algorithm	30
3.2.3. Limiter	31
3.2.4. Time Integration	31
3.3. Grid Generation	31
3.4. Flow Solver: GASPex	33
3.4.1. Boundary and Initial Conditions	33
Boundary Conditions	33
Initial Condition	35
3.4.2. Space Discretization	35
3.4.3. Time Integration	35
3.4.4. Post Processing	36
3.5. Computing Resources	36
3.6. Validation	36
4. Results	39
4.1. Numerical Results for Different Cases	39

4.1.1. Steady State	40
4.1.2. Stochastically Stationary State	40
4.1.3. Visualization of Flow	41
Case 1 : Infinitely Long Filament	41
Case 2: Finite Multiple Filaments ($L/D = 4/3$)	43
Case 3 : Finite Multiple Filaments ($L/D = 2$)	44
Case 4 : Finite Multiple Filaments ($L/D = 4$)	45
4.1.4. Drag Reduction Effectiveness and Efficiency	46
Formulation	47
Results	49
5. Conclusions - Future Work	68
6. Numerical Schlieren	70
References	71
Vita	74

List of Tables

2.1. Governing Dimensionless Parameters	18
2.2. Studied Cases	18
4.1. Studied Cases	39
4.2. Case 1	41
4.3. Case 2	43
4.4. Case 3	44
4.5. Case 4	46

List of Figures

1.1. MW Filaments [6]	2
1.2. Schematic diagram of MW equipment used in breakdown studies in air [26]	4
1.3. Experimental set-up at Saint Petersburg University	5
1.4. a)The wave guide b)The chamber test with aluminum strips to focus the MW beam.	5
1.5. Numerical simulation of the flow structure during the interaction of a hot filament with cylinder shock layer [9]	7
1.6. The effect of MW energy deposition on a blunt body at $M_\infty = 2.1$	8
1.7. MW installation in IVTAN [7]	10
1.8. The computed surface pressure on the centerline	11
1.9. The single energy impulse interaction with the sphere at $M_\infty = 3.45$, $t =$ 70μ s: a) calculated density gradients. b) experiment	13
1.10. The pulsed energy deposition in front of a spherical blunted body at $M_\infty = 2$: a) calculated density gradients. b) experimental shadowgraphs	14
1.11. The pulsed energy deposition in front of a conically sharp body at $M_\infty = 2$: a) calculated density gradients. b) experimental Schlieren images	15
2.1. Schematic sketch of the problem	17
3.1. Cells used to define $Q_i(x)$	24
3.2. The meshed field	32
3.3. The boundary conditions	34
3.4. The steady state dimensionless density field	37
4.1. The steady state density field	50
4.2. Infinitely long filament a) Mean pressure at the centerline, b) Pressure fluc- tuations at the centerline	51

4.3. $L/D = 4/3$, a) Mean pressure at the centerline, b) Pressure fluctuations at the centerline	51
4.4. $L/D = 2$, a) Mean pressure at the centerline, b) Pressure fluctuations at the centerline	52
4.5. $L/D = 4$, a) Mean pressure at the centerline, b) Pressure fluctuations at the centerline	52
4.6. The density field for the interaction of infinitely long filament with the shock layer	53
4.7. The pressure field for the interaction of infinitely long filament with the shock layer	54
4.8. Numerical Schlieren images for the interaction of infinitely long filament with the shock layer	55
4.9. The density field for the interaction of the train of finite filaments with the shock layer($L/D = 4/3$)	56
4.10. The pressure field for the interaction of the train of finite filaments with the shock layer($L/D = 4/3$)	57
4.11. Numerical Schlieren image for the interaction of the train of finite filaments with the shock layer($L/D = 4/3$)	58
4.12. The density field for the interaction of the train of finite filaments with the shock layer($L/D = 2$)	59
4.13. The pressure field for the interaction of the train of finite filaments with the shock layer($L/D = 2$)	60
4.14. Numerical Schlieren image for the interaction of the train of finite filaments with the shock layer($L/D = 2$)	61
4.15. The density field for the interaction of the train of finite filaments with the shock layer($L/D = 4$)	62
4.16. The pressure field for the interaction of the train of finite filaments with the shock layer($L/D = 4$)	63

4.17. Numerical Schlieren image for the interaction of the train of finite filaments with the shock layer($L/D = 4$)	64
4.18. The amount of drag reduction for: a) infinitely long filament b) $L/D = 4/3$ c) $L/D = 2$ d) $L/D = 4$	65
4.19. The drag reduction efficiency for: a) infinitely long filament b) $L/D = 4/3$ c) $L/D = 2$ d) $L/D = 4$	66
4.20. Asymptotic values for effectiveness	66
4.21. Asymptotic values for efficiency	67
4.22. Drag reduction efficiency vurses effectiveness	67

Chapter 1

Introduction

1.1 Motivation

Most high speed aircraft are blunt-nosed rather than sharp-nosed to reduce surface heating. As the flight speed increases this advantage is more evident. However, blunt-nosed vehicles have higher drag than sharp-nosed ones. Thus, the study of methods to reduce the drag on the blunted bodies becomes necessary.

There exist several aerodynamic methods to redirect the stream at supersonic speeds by means of separation and circulation which lead to drag reduction on blunt bodies. Such a flow can be created by means of a mechanical spike mounted on the blunt body [8, 29]. In supersonic flows, weak perturbations produced by local changes in temperature or density were shown to effectively modify the bow shock and reduce the aerodynamic drag on blunted bodies. These local changes could be created by means of various kinds of energy discharges such as laser, microwave (MW), glow, *etc.* (for example, see, [1, 4, 5]). For MW energy deposition, the physical mechanism for drag reduction is the interaction of the thin hot filaments with the shock structure generated by the body (Figure 1.1). In the present research, the effect of pulsed MW energy addition on drag reduction for a cylinder is examined.

Application of the MW technique is not the easiest way to obtain discharge in air-flow. This technique is more complicated than some other methods such as DC discharge. However, there are some options available by using MW discharge that makes it more advantageous for applications in flow control. These options are, namely, capability for action in distance, energy delivery at the speed of light at a defined point, electronic control of the MW beam focus shape and orientation according to the mission requirements and high efficiency of generation.



Figure 1.1: MW Filaments [6]

1.2 Literature Survey

There have been many of both experimental and numerical studies to investigate the application of energy deposition in aerodynamic flow control at supersonic speeds. Several review papers are available summarizing the recent studies: Knight *et al* [15, 16, 17], Zheltovodov *et al* [32] and Bletzinger *et al* [5]. In this section, some papers along with their important results are presented to provide the reader with some background regarding historical overview, experimental and numerical research.

1.2.1 Historical Overview

The idea of focusing of electromagnetic beams for distant energetic coupling with a gas flow appeared in the 1960's and was stimulated by rapid progress in MW and laser techniques. Despite many optimistic expectations regarding the application of electromagnetic beams in aerodynamics, more realistic ones were evident by recognizing the complexity of such systems and also by not obtaining rapid progress in efficiency. By the late 1970's and the beginning of the 1980's, another area emerged which later was named plasma aerodynamics. Plasma aerodynamics proved to be the catalyst which led to both reexamination of the phenomena and to the discovery of new phenomena in several basic disciplines such as gas discharge, gas dynamics and kinetic processes. Its brief description can be given by non-stationary, non-uniform or non-equilibrium behavior.

Many interesting events occur when an electromagnetic field is applied to a gas medium. The study of electromagnetic discharges in gases has led to many fundamental discoveries.

A small segment of this field is related to electric breakdown at high frequencies which dates back to the end of World War II. The term breakdown corresponds to the initiating process and seemed reasonable to those studying the phenomena in which a DC voltage across a gas tube was gradually increased until the gas suddenly started to glow and became conducting.

The development of radar during the World War II led to the improvement of MW techniques. Once a high-frequency field is applied across a gas, the electrons travel short distances before the direction of the field changes. Therefore, electrons are not swept out of the discharge region by the field, but leave with relatively low speeds and produce no secondary effects at the surfaces of the container. There has been considerable experimental work among which one of the pioneer ones is presented here. This experiment is chosen so that it indicates in a general way the kind of experiments which were done [26]. Also, one of the current experiment set-ups in Saint Petersburg is described.

Figure 1.2 shows a schematic diagram of an arrangement to measure breakdown in atmospheric gases at a MW frequency of 10 GHz. MW power, stable in frequency and controllable in power level, reaches the resonant cavity by a waveguide from the magnetron source. A ferrite isolator prevents frequency pulling of the magnetron by the load by introducing about 10 db attenuation for signals traveling from load to source without significantly reducing the power transmission to the cavity. A small fraction of the power is led to the frequency-measuring system, which includes a frequency counter that allows accuracy to seven or eight significant figures. A known fraction of the power is also led to the calorimetric power meter using a calibrated directional coupler. A spectrum analyzer monitors the power transmitted through the cavity and serves to indicate when breakdown has taken place. A number of E-H tuners are used to ensure proper matching at certain points in the transmission line.

When the gas is introduced into the cavity at any desired concentration, the breakdown field is determined by gradually raising the power level, while keeping the source frequency at the resonant frequency of the cavity, until the gas in the cavity breaks down. The indication of breakdown is a sudden decrease of transmitted power caused by the gas becoming conducting and absorbing most of the power.

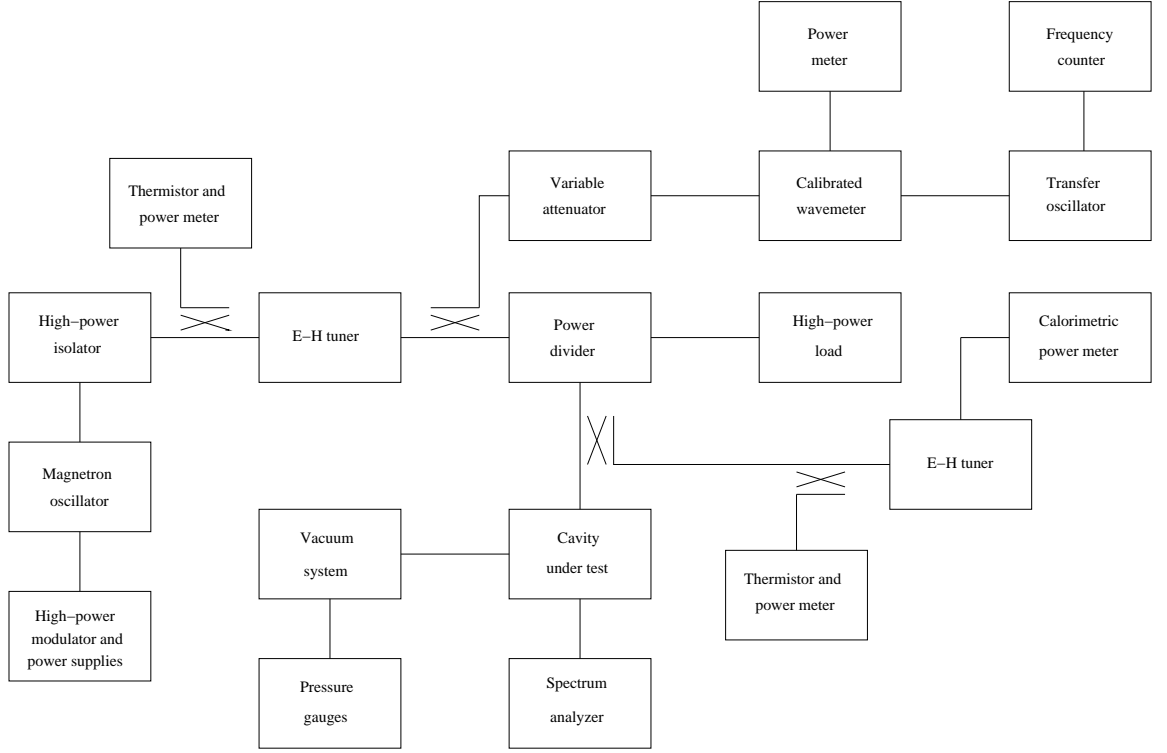


Figure 1.2: Schematic diagram of MW equipment used in breakdown studies in air [26]

Since breakdown is the result of an increase in electron concentration, there must be some electrons in the cavity when the field is applied; these are generally supplied by keeping a small radioactive source near the cavity.

MW breakdown depends on the purity of the gas being studied. Advances in vacuum technology have therefore been closely connected with progress in breakdown studies. For example, ultrahigh-vacuum techniques made it possible to attain pressures in a reasonably sized systems as low as 10^{-10} Torr in a matter of hours.

There have been many experimental studies of MW energy deposition for flow control at supersonic speeds. Here, as an example, we describe the experimental set-up at Saint Petersburg University. Figure 1.3 shows the components of the equipment including the waveguide, the test chamber, the parabolic mirror to focus the MW beam which was used before and the aluminum strips to focus the MW beam which are used now. The MW pulse once generated is directed to the chamber test via the wave guide and is focused on the desired point ahead the model using the aluminum strips. Closer views of the wave guide and the test chamber are shown in Figure 1.4.

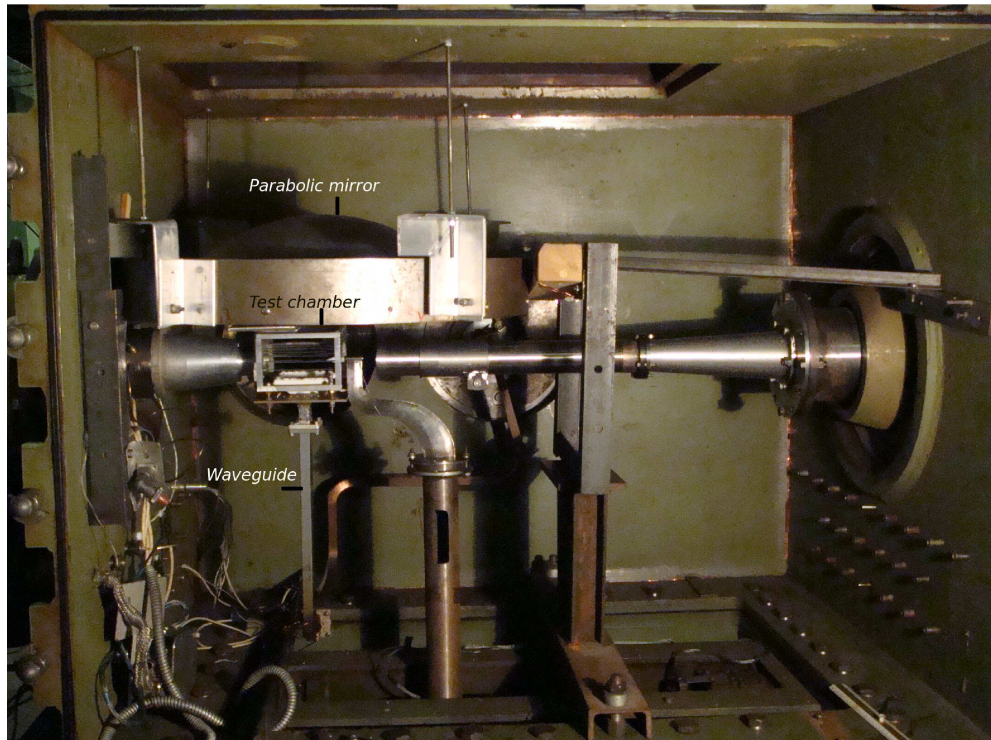
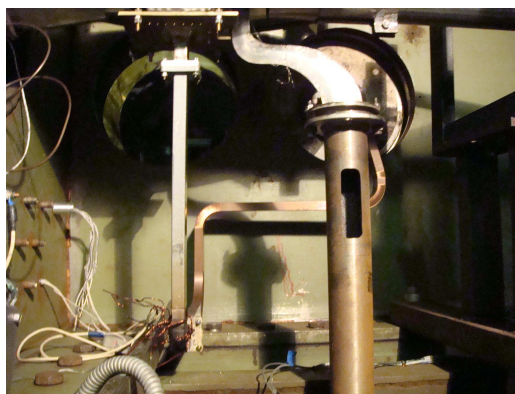
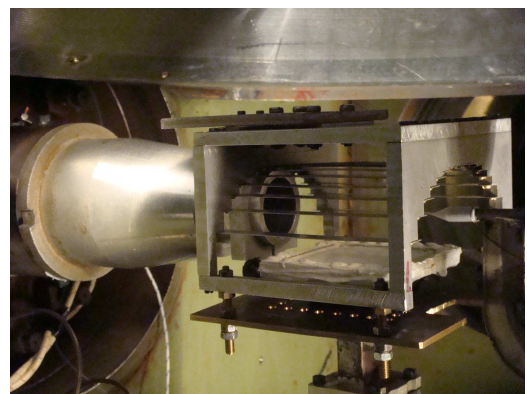


Figure 1.3: Experimental set-up at Saint Petersburg University



a)



b)

Figure 1.4: a)The wave guide b)The chamber test with aluminum strips to focus the MW beam.

1.2.2 Experimental Articles

The area is rich in experimental work. Different geometries of bodies have been studied through experimental set-ups and the effects of different parameters such as the dimension of the high temperature region, its strength in terms of the ratio of its density to the ambient density and its orientation with respect to the axis of the body have been investigated. Similar conclusions have been drawn regarding the phenomena observed: a vortex region within the shock layer is formed which reduces frontal drag by effective streamlining of the body (Figure 1.5). Also the stand-off distance of the bow shock and its shape change due to the interaction. The effect of the interaction on the flow structure and aerodynamic characteristics is shown to get magnified as the strength of the hot region and its length increase. Here, we mention a selected series of recent experiments.

Kolesnichenko *et al* 2001

Kolesnichenko *et al* [19] performed a series of experiments to study the effect of MW energy deposition on supersonic flow around an cylindrical body of diameter 8 mm in air, nitrogen, argon and carbon dioxide. The air flow is generated by means of central supersonic conical nozzle with exit Mach number of 1.5. The outer supersonic nozzle, gas ejector was set up to obtain a rarefaction in the working chamber. The following parameters of the working flow have been obtained: static pressure typically 60 Torr, Mach number 1.5 – 1.8 and static temperature typically 200 K. The MW unit is a klystron-type generator of high power pulses with X-range frequency. The ultimate pulse power attained is 210 kW. The pulse duration is 1.2 – 2.2 μ s. The pulse frequency can be as high as 1.0 kHz. The maximum mean power of the MW facility is about 400 W.

The Schlieren images of the interaction are provided. To investigate the influence of plasmoids on the drag, the surface pressure is measured on the centerline of the cylinder. A significant reduction in the surface pressure resulting in a momentary decrease in frontal drag is recorded. Investigation of spatial-temporal and spectral characteristics of light emission of MW discharge is carried out by two measuring channels and the detailed spatial-temporal data of discharge domains evolution and interaction are obtained.

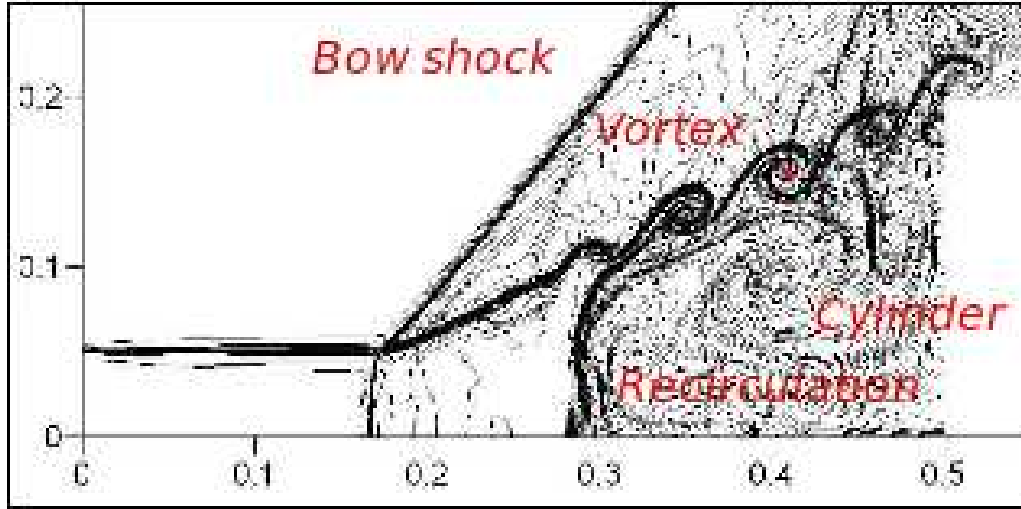


Figure 1.5: Numerical simulation of the flow structure during the interaction of a hot filament with cylinder shock layer [9]

Lashkov *et al* 2003, 2004

Lashkov *et al* [22, 23] performed a series of experiments to investigate the effect of MW energy deposition on blunt and hemisphere cylinders at $M_\infty = 2.1$, static pressure $p_\infty = 25$ Torr and static temperature $T_\infty = 159.4$ K. The wind tunnel is a free jet configuration. They studied a symmetric flow with the MW beam located approximately 70 – 90 mm from the jet nozzle exit. They provided Schlieren images and chemiluminescent imaging and surface pressure measurements. The initial lensing forward of the shock as the thermal region convects to the bow shock has been observed (Figure 1.6). The formation of a vortex region and transient streamlining of the flow past the body resulting in a decrease in frontal pressure have been pointed out. The effect of off-axis position of the MW beam is also examined for the case of a hemisphere body. It is shown that for some larger distance from the axis of the body, energy deposition actually increases the drag.

Mashek *et al* 2004

There are also experiments performed to combine existing methods with MW deposition to investigate the possibility of the MW beam generation in atmospheric pressure. In their work, Mashek *et al* [27], set up several experiments to study MW discharge initiated by a laser spark. Their objective is to ascertain the capability of a laser spark to act as a

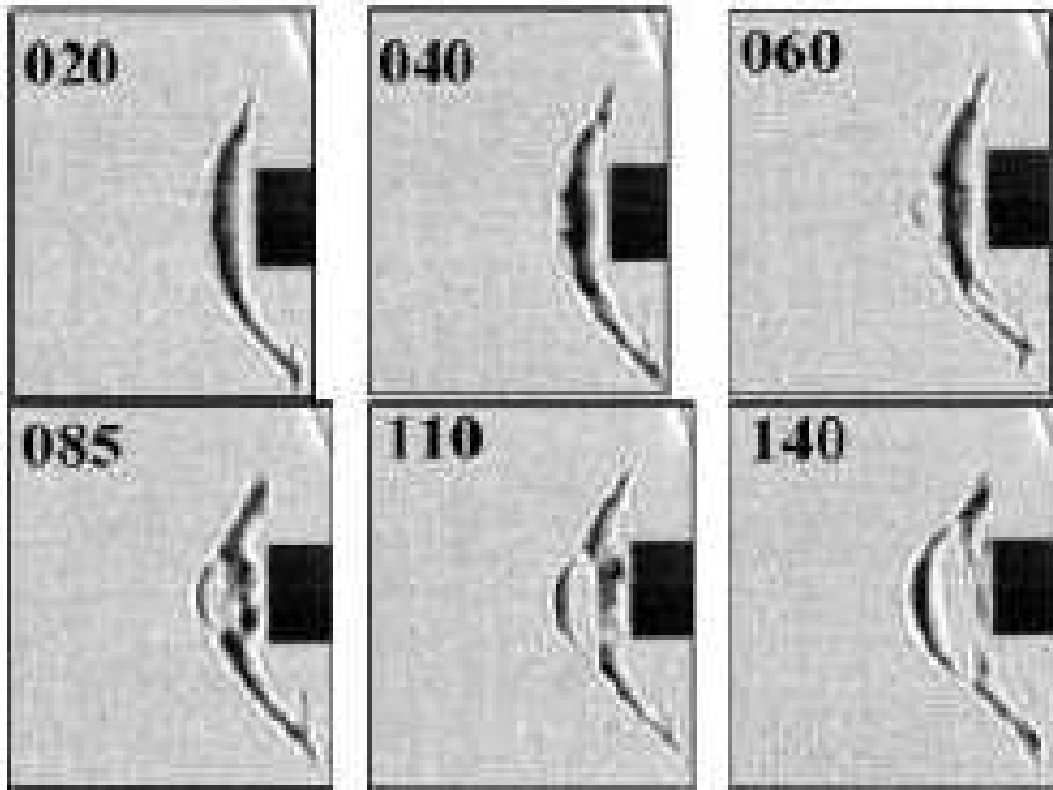


Figure 1.6: The effect of MW energy deposition on a blunt body at $M_\infty = 2.1$

precursor (initiator) for MW discharge in air at atmospheric pressure. The laser spark is created by an impulse ruby laser in the focal point of short-focus lens (12 mm). The X-range impulse MW generator with output power 180 kW and pulse duration $1.2 \mu\text{s}$ via radiating system illuminates the focal area. A digital synchronous Schlieren system is used for visualization of the shock wave structures excited by the laser spark and initiated by the MW discharge. The luminosity of discharges is measured by fast photo multiplier tubes with a time resolution better than 30 ns. According to their results, one can create MW discharge at atmospheric pressure using laser precursor. They also examined the effect of different delay times between the MW and laser to attain the maximum luminosity which is shown to be $80 - 110 \mu\text{s}$ and the duration of this discharge is defined by the MW impulse.

Brovkin *et al* 2006

Brovkin *et al* [7] carried out an experimental investigation of combined laser-DC-MW discharges. The operations were conducted using a powerful MW generator of magnetron type (700 kW, 13 GHz), pulsing laser Nd:YAG (532 nm, 130 mJ/pulse) and pulsing DC source (Figure 1.7). It was observed that at the reduced pressure the threshold of initiation of the MW discharge is essentially decreased by the laser radiation even without laser-induced spark generation. The opportunity of remote generation of the MW discharge is shown. Special attention was given to studies of the interaction process of the MW discharge with a laser plasma and the gas medium distributed by it at the late stages of decay. The results also point out the potential of adjustment of the process of energy deposition by means of changes in delays, and also the intensity levels of the MW and laser radiation.

1.2.3 Numerical Articles

Kolesnichenko *et al* 2002

Some preliminary results of numerical simulations based on the Euler equations of the interaction of a heated channel with a two-dimensional blunt body at $M_\infty = 1.9$ are presented in this work [20]. Different diameters of the model are studied and it is shown



Figure 1.7: MW installation in IVTAN [7]

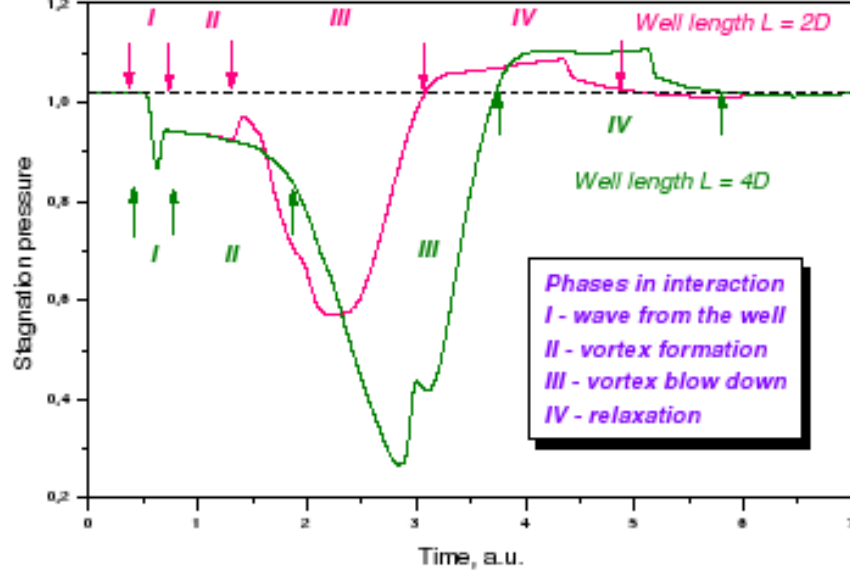


Figure 1.8: The computed surface pressure on the centerline

that the peak value of stagnation pressure reduction increases with the model diameter. The lensing forward of the shock due to the initial interaction, the formation of a vortex pair, recirculation region and reflected shock waves inside the shock layer are displayed via computed Schlieren images. Four phases are assigned to the changes in surface pressure: phase *I* relates to pressure drop because of expansion wave generated by the interaction, phase *II* refers to significant pressure drop due to vortex generation and also is associated with momentarily effective streamlining of the body due to the creation of recirculation area ahead the body. Phases *III* and *IV* correspond to the convection of the vortex past the body and the recovery of pressure to its undisturbed level respectively (Figure 1.8).

Kolesnichenko *et al* 2003

Kolesnichenko *et al* [18] developed a model for the formation time of the hot filament. The analytical model yields a finite time collapse-like creation of a hot plasma channel with high electron concentration and temperature. The formation time of the hot channel is:

$$t_{channel} = [1.5k^2\eta\sigma_0E_0^2\rho_0^{-1}]^{-1/3}$$

where k is proportional to the MW wave number, η is the fraction of the dissipated energy transformed into heating of the gas, σ_0 is the conductivity, E_0 is the amplitude of the electric

field and ρ_0 is the ambient density. For typical values ($\sigma_0 = 100$ Siemens, $\lambda = 3$ cm, $p_0 = 76$ Torr, $E_0 = 3$ kv/cm), the model predicts $t_{channel} = 1 \mu s$ in agreement with experiment.

Azarova *et al* 2005

In this paper [2], a numerical study based on the Euler equations is performed for wedge-shaped bodies at different angles and different positions of MW discharge. Flow structure, stagnation parameters, drag forces, stand-off distance and the shape of bow shock in the case of an infinitely long filament are examined. For certain angles of the wedge, the detached wave is observed and additional strong shock or acoustic waves (depending on the angle) are generated within the shock layer and later join the bow shock. Dividing or not dividing the vortex region near the top corner of the body depends again on the angle of the wedge. For the cases of attached bow shock, no additional shock waves are formed and only an acoustic wave traveling to the bow shock is observed. In addition, the vortex region is not divided in these cases. Some flow structures can be pointed out in both categories (detached and attached bow shock) such as the deformation of bow shock, the increase in its stand-off distance, the generation of weak shocks moving to the right on top surface of the body and significant decrease in frontal drag which is less for detached cases. Generally, the effects become stronger as the degree of rarefaction of the hot filament or its length increases.

Lashkov *et al* 2006

In a paper by Lashkov *et al* [21] a simplified analysis of gas motion at the beginning of the interaction is offered and a list of main dimensionless parameters of this motion such as the Mach number of flow, the heating degree and geometric parameters is discussed. The results of numerical modeling on the basis of the Euler equations for a cylindrical aerodynamic body with a complicated cavity to examine the possibility of intensifying the vortex region are provided. The calculation analysis showed that the presence of the cavity in the cylinder body amplifies the effects of drag force reduction. The effects established are stronger for longer channels or for higher degrees of rarefaction. It is also pointed out that

there exist time intervals in which the effects do not depend on the radius of the channel but only on its length.

Zheltovodov *et al* 2007

Zheltovodov *et al* [33] have provided numerical calculations on a basis of 2-D axisymmetric unsteady Euler equations and have compared the results with some known experiments with laser induced energy deposition located upstream of different bodies. In their work, the interaction of single pulse with a sphere at $M_\infty = 3.45$ has been studied and the complex unsteady flow structure is analyzed (Figure 1.9). Furthermore, the results of parametrical numerical research of the flowfield features in the vicinity of blunt spherical and sharp conical axisymmetric bodies in the case of periodic pulsed energy deposition in argon is performed at $M_\infty = 2$ (Figures 1.10 and 1.11). Comparison of performed calculations with known experimental results confirms the reliability of such an approach to predict some important features of the flowfield such as the deformation of the bow shock, the formation of contact discontinuities and the lensing effect of the interaction in different cases. Also, the main tendencies of drag reduction for spherical and conical bodies under energy deposition influence have been demonstrated and specified.

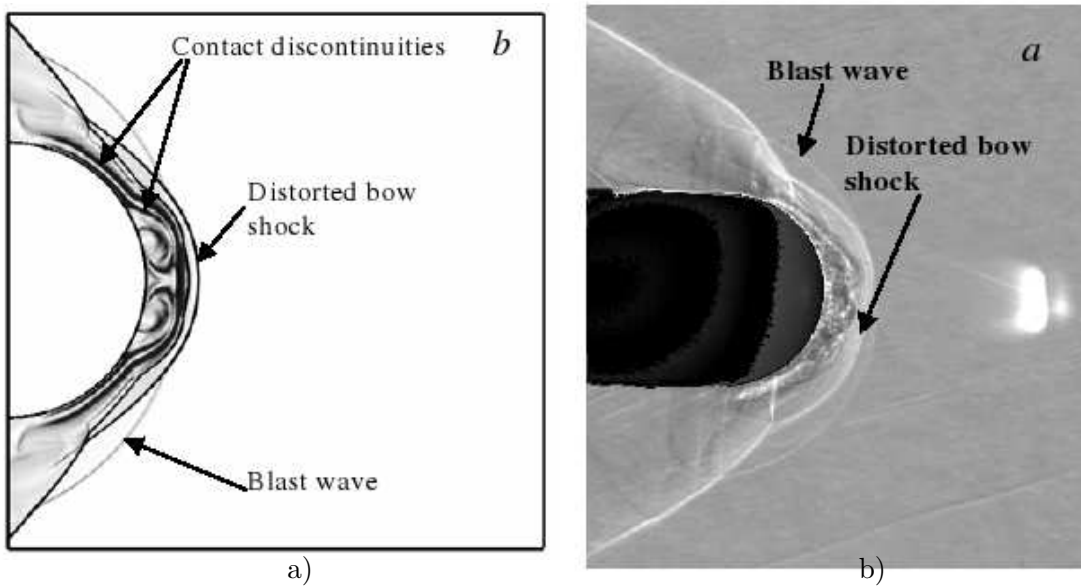


Figure 1.9: The single energy impulse interaction with the sphere at $M_\infty = 3.45$, $t = 70\mu$ s: a) calculated density gradients. b) experiment

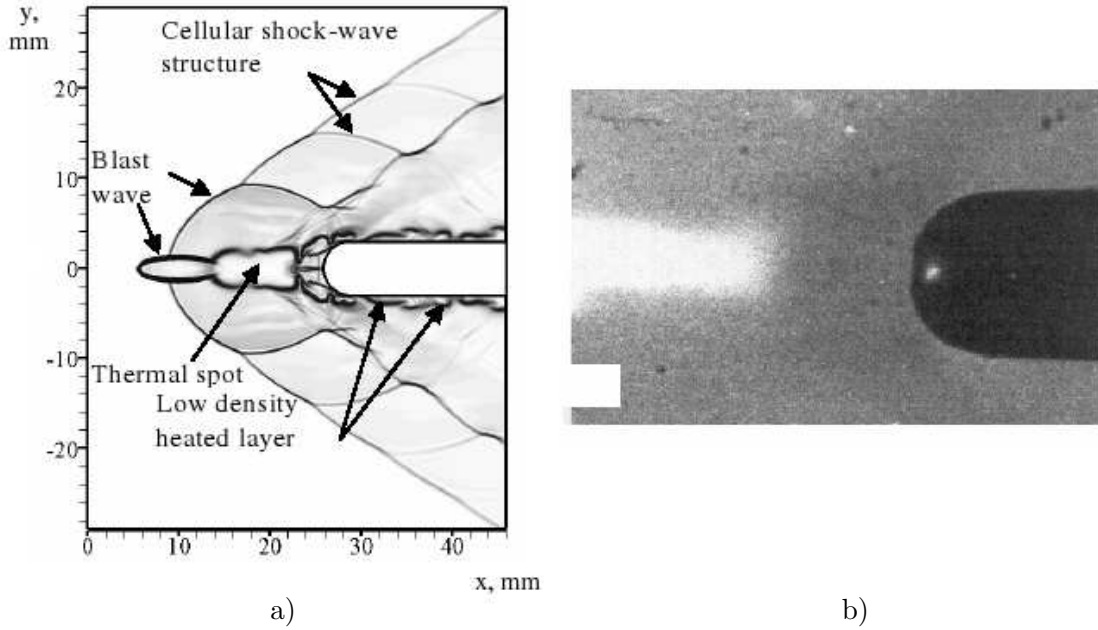


Figure 1.10: The pulsed energy deposition in front of a spherical blunt body at $M_\infty = 2$: a) calculated density gradients. b) experimental shadowgraphs

1.3 Statement of Objectives

In this work, the interaction of a heated filament with the shock layer ahead of a cylinder is studied. The heated filament is a simplified model of the plasma filament generated by a MW discharge (Figure 1.1). The main flow structures which are generated due to the interaction are investigated and the behavior of the flow is studied by analyzing different contours such as pressure and density fields. Furthermore, examining the effect of different parameters in the effectiveness as well as in the efficiency of the pulsed energy deposition in drag control is of main interest. Effectiveness is the percent of drag reduction caused by the interaction of a train of finite filaments with the shock system; however, the amount of drag reduction itself is not a sufficient measure and the calculation of the efficiency of the process is needed as well, *i.e.*, the ratio of the drag power saved to the power expended to produce the MW filaments.

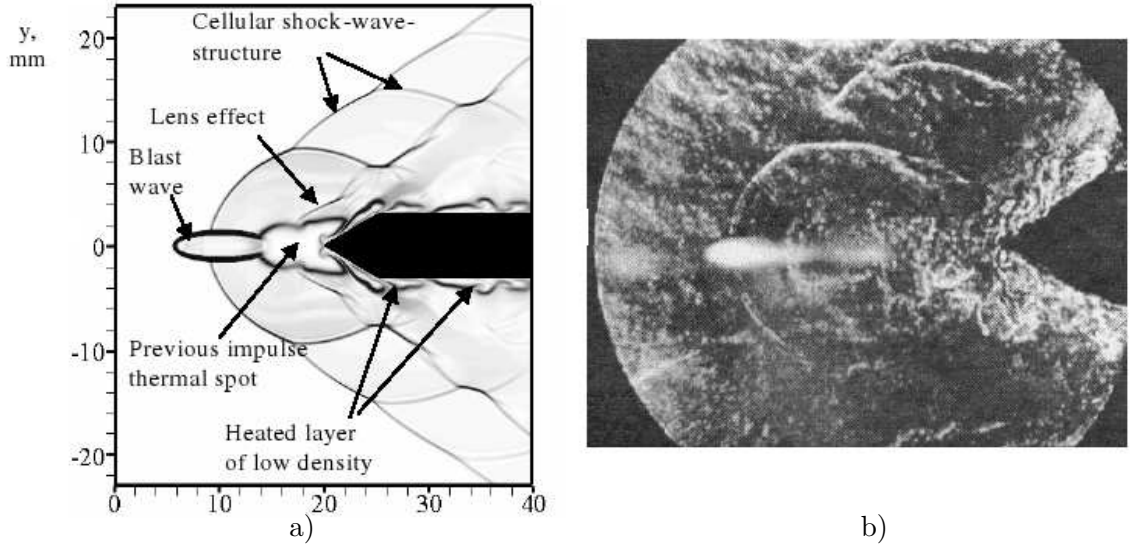


Figure 1.11: The pulsed energy deposition in front of a conically sharp body at $M_\infty = 2$: a) calculated density gradients. b) experimental Schlieren images

1.3.1 Outline of the Thesis

Chapter 2 introduces a schematic sketch of the problem, the governing dimensionless parameters and the parameters of interest which are investigated in this work. The methodology including the governing equations, the numerical algorithms and grid generation is discussed in Chapter 3. The description of the CFD code can also be found in this chapter. The results from the flow solver representing the flow structure are presented in Chapter 4. Further analysis to study the capability of introducing pulsed filaments into the shock system to control the drag, is performed and described in this chapter. In the final section conclusions and future work studies are summarized.

Chapter 2

Problem Statement

2.1 Problem Definition

A sketch of the flow configuration is shown in Figure 2.1. Consider a cylinder in a supersonic flow. A bow shock wave is created in front of the body. Using pulsed energy addition, a region of high temperature and consequently low density is created in front of the bow shock. This region is called a “temperature spot” or “density well”. Within this region, there exists a weakly ionized medium containing visible filaments of diameter $d \approx 0.1\text{--}1$ mm and length of $l \approx 10\text{--}30$ mm [19] (Figure 1.1). In the current research, the filaments are modeled as a thermal effect and therefore as tiny cylinders of high temperature aligned with the body’s axis.

These filaments travel with the same speed as the flow and as they approach¹ and interact with the bow shock, they deform its shape and therefore the flow structure and pressure behind the bow shock changes due to this interaction. The objective of this work is to examine the change in the flow structure and the pressure on the aerodynamic body caused by the interaction of infinite or finite MW pulses with the cylinder shock system.

¹The pressure inside the filament is the freestream pressure, *i.e.*, p_∞ .

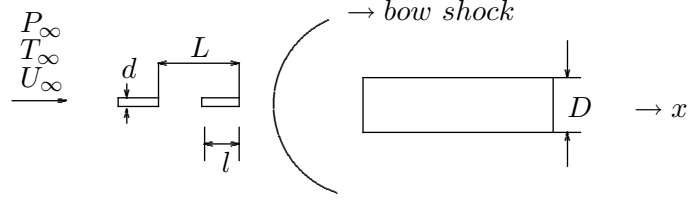


Figure 2.1: Schematic sketch of the problem

2.2 Dimensionless Parameters

There are two dimensionless parameter associated with the aerodynamic properties of the flow which are the Mach number², M_∞ , and the ratio of the density in the filament to the freestream density, α . In nondimensionalizing, there are also three additional dimensionless lengths associated with the geometry of the filaments, namely the filament length (l/D), diameter (d/D) and spacing (L/D). The governing dimensionless parameters are listed in Table 2.1. The geometric parameters³ are defined in Figure 2.1.

According to experiments (see, for example, [19]), the typical diameter for the filament is $d \approx 0.1 - 1$ mm and again from the similar experiments, the aerodynamic body's diameter is typically $D \approx 10 - 40$ mm. Thus, $0.0025 \leq d/D \leq 0.1$ and the choice of $d/D = 0.1$ represents a typical experiment. Similarly, the typical length for the filament is $l \approx 10 - 30$ mm and the selected value, $l/D = 1.0$, falls in the appropriate range. The values for M_∞ and α which are listed in Table 2.1 are chosen such that they are consistent with the experiments.

2.3 Parameters Investigated

The specific objective of this research is studying the effect of altering the period, L/D , of the pulsed filaments on drag reduction. For this purpose, all other parameters are kept fixed after assigning appropriate values to them. Four different cases are examined which are listed in Table 2.2.

²Mach number is defined as $M_\infty = U_\infty/a_\infty$, where U_∞ is the freestream velocity and a_∞ is the freestream speed of sound. For a perfect gas, $a = \sqrt{\gamma RT}$.

³The Mach number of the filament is $\sqrt{\alpha}M_\infty$

Type	Description	Definition	Value
Flow	Mach	M_∞	1.89
	Specific heats ratio	γ	1.4
Filament	Density ratio	α	0.5
	Diameter	$\frac{d}{D}$	0.10
	Length (Duration ⁴)	$\frac{l}{D}$	varies
	Pulse (Period)	$\frac{L}{D}$	varies

^b The temporal duration of a pulse, non-dimensionalized by $\frac{D}{U_\infty}$, is $\frac{l}{D}$. Likewise, the pulse period is $\frac{L}{D}$ for the same non-dimensionalization.

Table 2.1: Governing Dimensionless Parameters

Case	Description	$\frac{d}{D}$	$\frac{l}{D}$	$\frac{L}{D}$
1	Infinitely long filament	0.10	∞	n/a
2	Finite multiple filaments	0.10	1.0	4/3
3	Finite multiple filaments	0.10	1.0	2
4	Finite multiple filaments	0.10	1.0	4

Table 2.2: Studied Cases

Chapter 3

Methodology

This chapter summarizes the governing equations, numerical algorithms, grid generation, computer tools and finally a validation for the code which is used for the computations. The governing equations of the problem are the unsteady axisymmetric Euler equations which are discussed in detail in Section 3.1. Also, a comprehensive review of the numerical algorithms applied is presented in Section 3.2 followed by the description of the grid in Section 3.3. In section 3.4, the CFD code employed to solve the flow is described. Finally, a steady-state case to demonstrate a validation for the solver code is presented.

3.1 Governing Equations

Fluid motion is governed by three major independent laws: conservation of mass (continuity equation), conservation of momentum (Newton's second law of motion) and conservation of energy. First, the assumptions on which the computations are based are specified:

1. Axisymmetric flow
2. Unsteady flow
3. Inviscid flow
4. Compressible flow
5. Neglect body force

Conservation of mass

$$\frac{\partial \rho}{\partial t} + \frac{\partial \rho u_k}{\partial x_k} = 0 \quad (3.1)$$

The momentum equation (Euler equation)

$$\frac{Du_i}{Dt} = -\frac{1}{\rho} \frac{\partial p}{\partial x_i} \quad (3.2)$$

where ρ is the density, u_i are the velocity components (u_1, u_2, u_3) in the Cartesian coordinate system (x_1, x_2, x_3) and p is the static pressure. $\frac{D}{Dt}$ is the convective derivative of a function and is defined as

$$\frac{D}{Dt} = \frac{\partial}{\partial t} + u_i \frac{\partial}{\partial x_i} \quad (3.3)$$

Finally the energy equation

$$\rho \frac{De}{Dt} = -\frac{\partial p u_k}{\partial x_k} \quad (3.4)$$

where $e = c_v T + 1/2(u_1^2 + u_2^2 + u_3^2)$.

There are four equations with five unknowns (ρ, u_1, u_2, u_3, e) in the above set of equations. In order to solve for the unknowns, another equation is needed which is the equation of state for thermally perfect gas which is $p = \rho R T$. In this equation, $R = c_p - c_v$, is the specific gas constant, where c_p is the specific heat at constant pressure and c_v is the specific heat at constant volume.

3.1.1 Nondimensionalization

To obtain the governing equations in dimensionless form, the nondimensionalization is done for the following:

1. The governing equations.
2. The boundary conditions.
3. The initial conditions.

Starting with the governing equations, nondimensionalization should be done for all the variables which appear in the problem

$$u_i^* = \frac{u_i}{U_{ref}}$$

$$\begin{aligned}
x_i^* &= \frac{x_i}{L_{ref}} \\
t^* &= \frac{t}{(L_{ref}/U_{ref})} \\
p^* &= \frac{p}{\rho_{ref} \cdot U_{ref}^2} \\
T^* &= \frac{T}{T_{ref}} \\
\rho^* &= \frac{\rho}{\rho_{ref}} \\
e^* &= \frac{e}{U_{ref}^2}
\end{aligned} \tag{3.5}$$

Now, the reference values used to nondimensionalize the variables listed above are specified (see Figure 2.1

$$\begin{aligned}
U_{ref} &= U_{\infty} \\
L_{ref} &= D \\
\rho_{ref} &= \rho_{\infty} \\
T_{ref} &= T_{\infty}
\end{aligned} \tag{3.6}$$

Therefore, one obtains:

$$\begin{aligned}
u_i^* &= \frac{u_i}{U_{\infty}} \\
x_i^* &= \frac{x_i}{D} \\
t^* &= \frac{t}{(D/U_{\infty})} \\
p^* &= \frac{p}{\rho_{\infty} U_{\infty}^2} \\
T^* &= \frac{T}{T_{\infty}} \\
\rho^* &= \frac{\rho}{\rho_{\infty}} \\
e^* &= \frac{e}{U_{\infty}^2}
\end{aligned} \tag{3.7}$$

3.1.2 Governing Equations in Dimensionless Form

The governing equations are taken and the variables are substituted with the dimensionless variables obtained above. Doing so, no dimensionless parameter will appear in the governing equations. Thus, the governing equations would be as follows

Conservation of mass

$$\frac{\partial \rho^*}{\partial t^*} + \frac{\partial \rho^* u_k^*}{\partial x_k^*} = 0 \quad (3.8)$$

The momentum equation (Euler equation)

$$\frac{Du_i^*}{Dt^*} = -\frac{1}{\rho^*} \frac{\partial p^*}{\partial x_i^*} \quad (3.9)$$

and finally the energy equation

$$\rho^* \frac{De^*}{Dt^*} = -\frac{\partial p^* u_k^*}{\partial x_k^*} \quad (3.10)$$

From now on, for simplicity, the superscript $*$ and is dropped and dimensionless variables are used in equations.

3.1.3 Boundary Conditions in Dimensionless Form

The boundary conditions in this problem are as follows (Figure 2.1)

1. Upstream velocity is U_∞ (for both inflow and the filament)
2. Upstream temperature is T_∞ (excluding the filament)
3. Upstream pressure is p_∞ (for both inflow and the filament)
4. Filament density is $\rho_f = \alpha \rho_\infty$

It is clear that by knowing two thermodynamic properties in the upstream flow (*e.g.*, pressure and temperature), the other properties, (*e.g.*, the density), are known from the equation of state or other thermodynamic properties.

Now, the boundary conditions are nondimensionalized by using the dimensionless variables

$$U_\infty^* = \frac{U_\infty}{U_\infty} = 1 \quad (3.11)$$

$$T_\infty^* = \frac{T_\infty}{T_\infty} = 1 \quad (3.12)$$

The nondimensionless form of boundary condition for pressure

$$p_{\infty}^* = \frac{1}{\gamma M_{\infty}^2} \quad (3.13)$$

3.1.4 The Integral Form of the Conservation Laws

The integral equation for conservation of mass, momentum and energy may be written in a compact vector notation as

$$\frac{\partial}{\partial t} \int_V Q dV + \oint_A (F \cdot \hat{n}) dA = 0 \quad (3.14)$$

where \hat{n} denotes the outward unit vector normal to the surface, Q is the vector of the conservative variables, F is the inviscid flux vector.

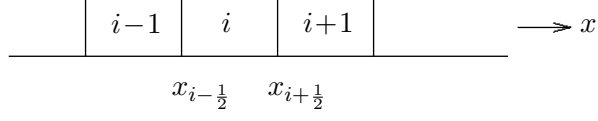
$$Q = \begin{Bmatrix} \rho \\ \rho u \\ \rho v \\ \rho w \\ \rho e \end{Bmatrix} \quad (3.15)$$

$$F \cdot \hat{n} = \begin{Bmatrix} \rho(\mathbf{V} \cdot \hat{n}) \\ \rho u(\mathbf{V} \cdot \hat{n}) + \hat{n}_x p \\ \rho v(\mathbf{V} \cdot \hat{n}) + \hat{n}_y p \\ \rho w(\mathbf{V} \cdot \hat{n}) + \hat{n}_z p \\ \rho H(\mathbf{V} \cdot \hat{n}) \end{Bmatrix} \quad (3.16)$$

where \mathbf{v} is the velocity vector and H is the total enthalpy which is defined as $H = e + \frac{p}{\rho}$.

3.2 Numerical Algorithm

The conservation equations (3.14) are applied to a discrete set of control volumes V_i . The solution requires specification of a set of control volumes and algorithms for the spatial and temporal quadratures. In this section, a detailed description of selected algorithms for both spatial and temporal discretization which are Van Leer's scheme and Runge–Kuta method

Figure 3.1: Cells used to define $Q_i(x)$

respectively, is provided. Everything is explained in one dimension and the expansion of the results to three dimension is straightforward. For the reader's convenience, here is the one dimensional form of Euler's equations

$$\frac{\partial}{\partial t} \int_V Q dx dy + \oint_A F dy = 0 \quad (3.17)$$

where the vector of dependent variables and inviscid fluxes are as follows

$$Q = \begin{pmatrix} \rho \\ \rho u \\ \rho e \end{pmatrix} \quad (3.18)$$

$$F = \begin{pmatrix} \rho u \\ \rho u u + p \\ \rho e u + p u \end{pmatrix} \quad (3.19)$$

Then Euler equations (3.17) are applied to a discrete set of control volumes (Figure 3.1), $V_i = \Delta x \Delta y$. For each volume i , the volume-averaged values of Q are taken

$$\mathbf{Q}_i(t) = \frac{1}{V_i} \int_{V_i} Q dx dy \quad (3.20)$$

The spatial (flux) quadrature involves faces $i + \frac{1}{2}$ and $i - \frac{1}{2}$. Denote

$$\mathbf{F}_{i+\frac{1}{2}} = \frac{1}{A_{i+\frac{1}{2}}} \int_{x_{i+\frac{1}{2}}} F dy \quad (3.21)$$

where $A_{i+\frac{1}{2}} = \Delta y$ is the surface area of the face at $x_{i+\frac{1}{2}}$. Then the Euler equations (3.17) become

$$\frac{d\mathbf{Q}_i \Delta x \Delta y}{dt} + (\mathbf{F}_{i+\frac{1}{2}} \Delta y - \mathbf{F}_{i-\frac{1}{2}} \Delta y) = 0 \quad (3.22)$$

Since V_i is assumed to be independent of time,

$$\frac{d\mathbf{Q}_i}{dt} + \frac{(\mathbf{F}_{i+\frac{1}{2}} - \mathbf{F}_{i-\frac{1}{2}})}{\Delta x} = 0 \quad (3.23)$$

This is the *semi-discrete* by which the Euler partial differential equations are transformed into a system of ordinary differential equations. Given the solution \mathbf{Q}_i for each cell's centroids at time t^n , the solution at time $t^{(n+1)}$ can be obtained by integration

$$\mathbf{Q}_i^{n+1} = \mathbf{Q}_i^n - \frac{1}{\Delta x} \int_{t^n}^{t^{n+1}} (\mathbf{F}_{i+\frac{1}{2}} - \mathbf{F}_{i-\frac{1}{2}}) dt \quad (3.24)$$

The problem is therefore reduced to defining the *temporal* and *spatial* quadrature algorithms for evaluating the second term on the right hand side of equation (3.24).

Also, the discretization of the domain and introduction of the volume averaged vector $Q_i(t)$ result in a loss of information regarding $\mathbf{Q}(x, t)$. The time evolution of Q_i requires, from (3.23) in the vicinity of $x_{i\pm 1/2}$ within each cell i , a local approximate *reconstruction* $Q_i(x)$ of the exact function $Q(x)$.

3.2.1 Flux Vector Splitting Method

Consider the semi-discrete form of Euler equation 3.23. Since the problem is one-dimensional, the flux $\mathbf{F}_{i+\frac{1}{2}} = F_{i+\frac{1}{2}}$. The basic idea behind flux vector splitting is to decompose the flux \mathbf{F} into two parts,

$$F = F^+ + F^-$$

where

$$\begin{aligned} \frac{\partial F^+}{\partial Q} &\text{has nonnegative eigenvalues} \\ \frac{\partial F^-}{\partial Q} &\text{has nonpositive eigenvalues} \end{aligned}$$

The term F^+ corresponds to waves that move from left to right across the cell interface and it is reasonable to use $Q_{i+\frac{1}{2}}^l$. Similarly, we will use $Q_{i+\frac{1}{2}}^r$ to evaluate F^- . There are several algorithms proposed for F^+ and F^- . In this work, Van Leer's method is utilized.

Van Leer's Method

Van Leer [13, 24] developed a flux vector split method based on the Mach number. The flux vector F can be written

$$F = \begin{pmatrix} \rho a M \\ \frac{\rho a^2}{\gamma} (\gamma M^2 + 1) \\ \rho a^3 M [\frac{1}{(\gamma-1)} + \frac{1}{2} M^2] \end{pmatrix} \quad (3.25)$$

The term involving the Mach number¹ is split into two parts, with ρ and a evaluated using Q^l or Q^r as appropriate. For the mass flux the term involving Mach number is simply M and is split according to

$$M = M^+ + M^- \quad (3.26)$$

The mass flux is taken to be

$$\rho u = \rho_l a_l M^+ + \rho_r a_r M^- \quad (3.27)$$

Van Leer proposed

$$M^+ = \begin{cases} 0 & \text{for } M \leq -1 \\ f_1^+ & \text{for } -1 \leq M \leq 1 \\ M & \text{for } M \geq 1 \end{cases} \quad (3.28)$$

and

$$M^- = \begin{cases} M & \text{for } M \leq -1 \\ f_1^- & \text{for } -1 \leq M \leq 1 \\ 0 & \text{for } M \geq 1 \end{cases} \quad (3.29)$$

where M is the average Mach number at the interface and may be defined as

$$M = \frac{u_l + u_r}{a_l + a_r} \quad (3.30)$$

¹Note that in this definition the Mach number can be positive or negative.

This yields

$$\rho u = \begin{cases} \rho_r a_r M & \text{for } M \leq -1 \\ \rho_l a_l f_1^+ + \rho_r a_r f_1^- & \text{for } -1 \leq M \leq 1 \\ \rho_l a_l M & \text{for } M \geq 1 \end{cases} \quad (3.31)$$

It remains to determine the functions f_1^+ and f_1^- . They are chosen to satisfy equation 3.26 and to provide continuity of M^\pm and its first derivative with respect to M at $M = \pm 1$. It can be shown that

$$\begin{aligned} f_1^+ &= \frac{1}{4}(M+1)^2 \\ f_1^- &= -\frac{1}{4}(M-1)^2 \end{aligned} \quad (3.32)$$

The complete expression for M^\pm are therefore

$$M^+ = \begin{cases} 0 & \text{for } M \leq -1 \\ \frac{1}{4}(M+1)^2 & \text{for } -1 \leq M \leq 1 \\ M & \text{for } M \geq 1 \end{cases} \quad (3.33)$$

and

$$M^- = \begin{cases} M & \text{for } M \leq -1 \\ -\frac{1}{4}(M-1)^2 & \text{for } -1 \leq M \leq 1 \\ 0 & \text{for } M \geq 1 \end{cases} \quad (3.34)$$

For the momentum flux, the term involving the Mach number is split according to

$$(\gamma M^2 + 1) = (\gamma M^2 + 1)^+ + (\gamma M^2 + 1)^- \quad (3.35)$$

The momentum flux is taken to be

$$\rho u^2 + p = \gamma^{-1} \rho_l a_l^2 (\gamma M^2 + 1)^+ + \gamma^{-1} \rho_r a_r^2 (\gamma M^2 + 1)^- \quad (3.36)$$

Van Leer proposed

$$(\gamma M^2 + 1)^+ = \begin{cases} 0 & \text{for } M \leq -1 \\ f_2^+ & \text{for } -1 \leq M \leq 1 \\ \gamma M^2 + 1 & \text{for } M \geq 1 \end{cases} \quad (3.37)$$

and

$$(\gamma M^2 + 1)^- = \begin{cases} \gamma M^2 + 1 & \text{for } M \leq -1 \\ f_2^- & \text{for } -1 \leq M \leq 1 \\ 0 & \text{for } M \geq 1 \end{cases} \quad (3.38)$$

This yields

$$\rho u^2 + p = \begin{cases} \gamma^{-1} \rho_r a_r^2 (\gamma M^2 + 1) & \text{for } M \leq -1 \\ \gamma^{-1} \rho_r a_r^2 f_2^- + \gamma^{-1} \rho_l a_l^2 f_2^+ & \text{for } -1 \leq M \leq 1 \\ \gamma^{-1} \rho_l a_l^2 (\gamma M^2 + 1) & \text{for } M \geq 1 \end{cases} \quad (3.39)$$

It remains to determine the functions f_2^+ and f_2^- . They are chosen to satisfy equation (3.35) and to provide the continuity of $(\gamma M^2 + 1)$ and its first derivative with respect to M at $M = \pm 1$. It can be shown that

$$\begin{aligned} f_2^+ &= \frac{1}{4}(M+1)^2[(\gamma-1)M+2] \\ f_2^- &= -\frac{1}{4}(M-1)^2[(\gamma-1)M-2] \end{aligned} \quad (3.40)$$

The complete expressions for $(\gamma M^2 + 1)^\pm$ are therefore

$$(\gamma M^2 + 1)^+ = \begin{cases} 0 & \text{for } M \leq -1 \\ \frac{1}{4}(M+1)^2[(\gamma-1)M+2] & \text{for } -1 \leq M \leq 1 \\ \gamma M^2 + 1 & \text{for } M \geq 1 \end{cases} \quad (3.41)$$

and

$$(\gamma M^2 + 1)^- = \begin{cases} \gamma M^2 + 1 & \text{for } M \leq -1 \\ -\frac{1}{4}(M-1)^2[(\gamma-1)M-2] & \text{for } -1 \leq M \leq 1 \\ 0 & \text{for } M \geq 1 \end{cases} \quad (3.42)$$

For energy flux, the term involving the Mach number is split according to

$$(\rho e + p)u = \rho_l a_l^3 M[(\gamma - 1)^{-1} + \frac{1}{2}M^2]^+ + \rho_r a_r^3 M[(\gamma - 1)^{-1} + \frac{1}{2}M^2]^- \quad (3.43)$$

Van Leer proposed

$$M[(\gamma - 1)^{-1} + \frac{1}{2}M^2]^+ = \begin{cases} 0 & \text{for } M \leq -1 \\ f_3^+ & \text{for } -1 \leq M \leq 1 \\ M[(\gamma - 1)^{-1} + \frac{1}{2}M^2] & \text{for } M \geq 1 \end{cases} \quad (3.44)$$

and

$$M[(\gamma - 1)^{-1} + \frac{1}{2}M^2]^- = \begin{cases} M[(\gamma - 1)^{-1} + \frac{1}{2}M^2] & \text{for } M \leq -1 \\ f_3^- & \text{for } -1 \leq M \leq 1 \\ 0 & \text{for } M \geq 1 \end{cases} \quad (3.45)$$

This yields

$$(\rho e + p)u = \begin{cases} \rho_r a_r^3 M[(\gamma - 1)^{-1} + \frac{1}{2}M^2] & \text{for } M \leq -1 \\ \rho_l a_l^3 f_3^+ + \rho_r a_r^3 f_3^- & \text{for } -1 \leq M \leq 1 \\ \rho_l a_l^3 M[(\gamma - 1)^{-1} + \frac{1}{2}M^2] & \text{for } M \geq 1 \end{cases} \quad (3.46)$$

It remains to determine the functions f_3^+ and f_3^- . They are chosen to satisfy (3.43) and to provide the continuity of $M[(\gamma - 1)^{-1} + \frac{1}{2}M^2]$ and its first derivative with respect to M at $M = \pm 1$. It can be shown that

$$\begin{aligned} f_3^+ &= \frac{1}{8}(\gamma + 1)^{-1}(\gamma - 1)^{-1}(M + 1)^2[(\gamma - 1)M + 2]^2 \\ f_3^- &= -\frac{1}{8}(\gamma + 1)^{-1}(\gamma - 1)^{-1}(M - 1)^2[(\gamma - 1)M - 2]^2 \end{aligned} \quad (3.47)$$

The complete expressions for $M[(\gamma - 1)^{-1} + \frac{1}{2}M^2]^\pm$ are therefore

$$M[(\gamma-1)^{-1} + \frac{1}{2}M^2]^+ = \begin{cases} 0 & \text{for } M \leq -1 \\ \frac{1}{8}(\gamma+1)^{-1}(\gamma-1)^{-1}(M+1)^2[(\gamma-1)M+2]^2 & \text{for } -1 \leq M \leq 1 \\ M[(\gamma-1)^{-1} + \frac{1}{2}M^2] & \text{for } M \geq 1 \end{cases} \quad (3.48)$$

and

$$M[(\gamma-1)^{-1} + \frac{1}{2}M^2]^- = \begin{cases} M[(\gamma-1)^{-1} + \frac{1}{2}M^2] & \text{for } M \leq -1 \\ -\frac{1}{8}(\gamma+1)^{-1}(\gamma-1)^{-1}(M-1)^2[(\gamma-1)M-2]^2 & \text{for } -1 \leq M \leq 1 \\ 0 & \text{for } M \geq 1 \end{cases} \quad (3.49)$$

3.2.2 Reconstruction Algorithm

As mentioned earlier, in a finite-volume code, the unknowns are stored as cell averages and the code uses these cell averages to reconstruct the point wise field. In current thesis, the higher-order point wise reconstruction is performed using the MUSCL (Modified Upwind Scheme for Conservation Laws) approach [13].

In the reconstruction function and face values, the discontinuities in Q should be considered. The attention may be restricted to the face values since they determine the flux at the cell face given the flux quadrature algorithm. The reconstruction within cell i may be written as

$$\begin{aligned} Q_{i+1/2}^l &= Q_i + \frac{1}{4}[(1-\kappa)\Delta Q_{i-1/2} + (1+\kappa)\Delta Q_{i+1/2}] \\ Q_{i-1/2}^r &= Q_i - \frac{1}{4}[(1-\kappa)\Delta Q_{i+1/2} + (1+\kappa)\Delta Q_{i-1/2}] \end{aligned} \quad (3.50)$$

where $\Delta Q_{i+1/2} = Q_{i+1} - Q_i$ and $\kappa = 1/3$. Equation (3.50) is then third order upwind-biased since $Q_{i+1/2}^l$ depends on Q_{i-1} , Q_i and Q_{i+1} , and thus $Q_{i+1/2}^l$ employs two cells on the left of $x_{i+1/2}$ and one cell to the right. Similarly, $Q_{i-1/2}^r$ depends on Q_{i-1} , Q_i and Q_{i+1} , and thus $Q_{i-1/2}^r$ employs two cells on the right of $x_{i-1/2}$ and one cell to the left.

3.2.3 Limiter

For every CFD calculation, a balance exists between accuracy, convergence and monotonicity. The solutions may possess any two of these quantities but not all three to the fullest extent. The monotonicity of the flow solution is controlled by limiters. In a paper, Godunov [11] showed that all monotone linear schemes can be at most of first-order accuracy. Hence, any linear procedure by which the gradients would be limited in second-order schemes will not fulfill the requested goal, and the only way around this difficulty is to introduce non-linear correction factors by limiter functions. The role of these limiters is to force the numerics to follow closely the variation bounded properties of Euler solutions. For the second order reconstruction, the limiter is chosen to be Min-Mod [12] with $\kappa = 1/3$.

3.2.4 Time Integration

An explicit second order method is applied, Runge-Kutta [13], for the temporal quadrature of the semi-discrete Euler equations 3.23. The two-stage Runge-Kutta algorithm is

$$\begin{aligned}
 Q_i^0 &= Q_i^n \\
 Q_i^1 &= Q_i^0 + \frac{\Delta t}{2} R_i^0 \\
 Q_i^2 &= Q_i^0 + \Delta t R_i^1 \\
 Q_i^{n+1} &= Q_i^2
 \end{aligned} \tag{3.51}$$

where we introduce the temporary vectors Q_i^0 , Q_i^1 and Q_i^2 . The temporary vector Q_i^0 is identified as Q_i^n . The first step computes an intermediate value Q_i^1 where R_i^0 implies evaluation using Q_i^0 . The second step computes the final value of Q_i^{n+1} with R_i evaluated using Q_i^1 . The vector Q_i^2 is identified as Q_i^{n+1} . The algorithm is temporally second-order, *i.e.*, the error in Q_i^{n+1} is $O(\Delta t^2)$.

3.3 Grid Generation

A structured algebraic grid is generated to discretize the physical domain. The code to generate the grid was developed in this research. The grid is in two-dimensional Cartesian

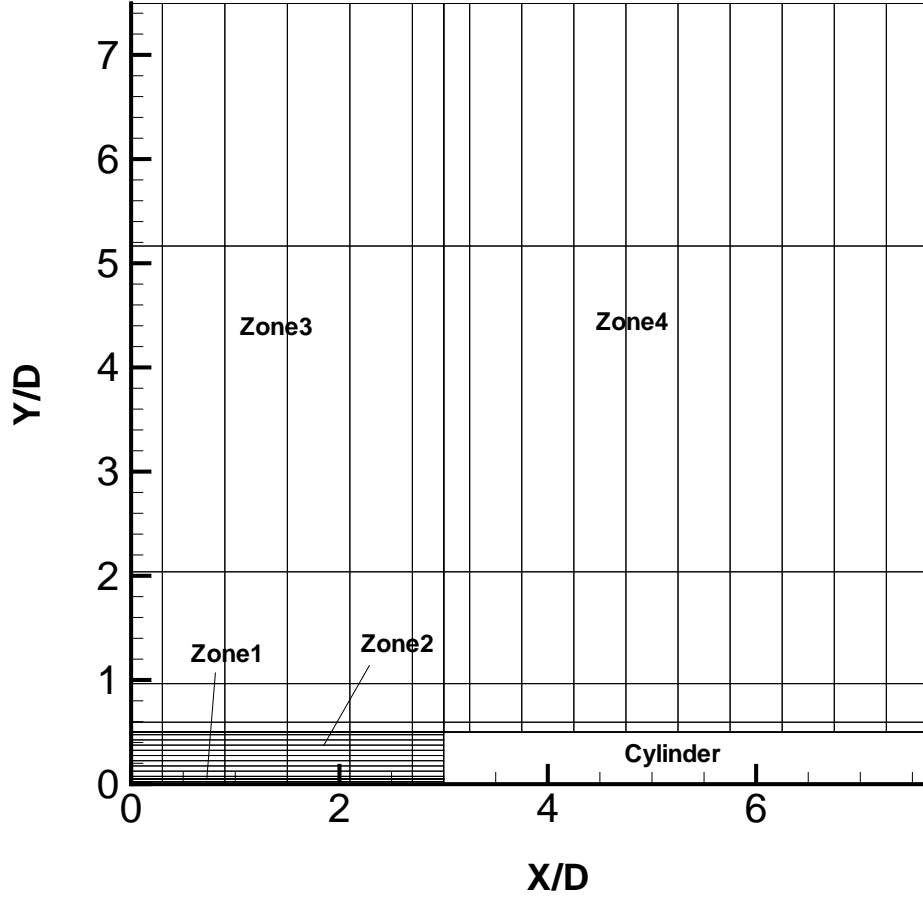


Figure 3.2: The meshed field

coordinate system; however, when it is imported in the flow code, the axisymmetric option is selected and the solver automatically converts the plane grid into an axisymmetric field. The original grid generation code is written in FORTRAN.

The total number of grid points is 356,800. The entire field is divided into four zones to apply proper grid spacing and boundary conditions. The meshed field is shown in Figure 3.2. For the purpose of visualization, not all the grid points are plotted.

3.4 Flow Solver: GASPex

All numerical algorithms described above along with importing the grid generated are applied through a flow solver in which the governing equations of the flow, namely conservation of mass, momentum and energy coupled with equation of state, are solved in a time accurate manner. In the analysis, the use of a commercial software which is verified against several test cases, GASPex [31], is made.

The General Aerodynamic Simulation Program (GASP) is a flow field analysis tool developed by Aerosoft Inc. GASP is written for the analysis of the structured multi-block grid systems of three dimensional flow domains. It solves the steady or time accurate Reynolds-Averaged Navier Stokes Equations (RANS) and its subsets, namely the Thin-layer Navier Stokes (TLNS), Parabolized Navier-Stokes (PNS), and Euler equations. GASP is written for compressible flow fields above Mach number of 0.1. This conservative shock capturing finite volume Computational Fluid Dynamics (CFD) code has a 6 degree of freedom (6-dof) motion modeling, and moving body simulation capability. It is possible to use a Chimera overlapping grid system which may be used for moving body simulations or for complex steady state simulations. Once the grid is imported, preparation of the input file for GASP includes three main types of information which will be supplied by the user, namely initial and boundary conditions, time and space discretization algorithms.

3.4.1 Boundary and Initial Conditions

Boundary Conditions

The appropriate boundary conditions to set up the model are applied using available options in GASPex.

Fixed at Q sets all boundary values according to a q specification, a q time, or point wise data. The energy release is modeled via the entrance boundary conditions ($x = 0$) as a finite or infinite channel of low density ρ_i , $\rho_i = \alpha\rho_\infty$ for $0 \leq r \leq d/2$ where d is the channel diameter, ρ_∞ is the density in undisturbed flow, and α is the degree of gas rarefaction in the channel. The other inflow parameters are equal to those of the undisturbed flow (Figure 3.3).

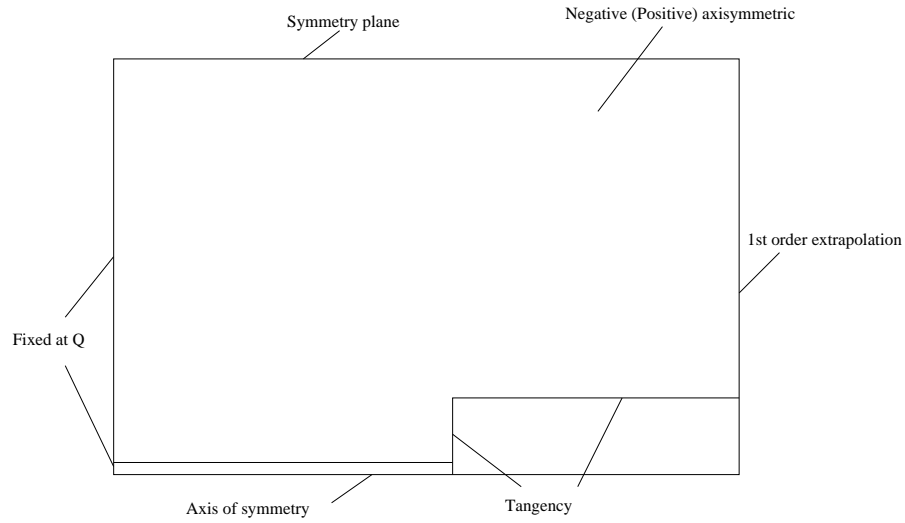


Figure 3.3: The boundary conditions

1st Order Extrapolation does a first order extrapolation from the interior cells for the boundary values. For the no-reflection condition on the exit, the boundary is set to be this type (Figure 3.3).

Negative (Positive) Axisymmetric Wall is an axi-symmetric side-wall boundary condition that assumes the flow is axi-symmetric, and that the singular axis is along the x axis. The angular displacement of the side walls must be exactly $\mp\pi/80$ or $\mp2.25^\circ$. The acute angle in a cross flow pie wedge must be exactly 4.5 (Figure 3.3).

Symmetry Plane assumes the flow is symmetric about the boundary face. There are no restrictions as to the surface orientation. This is the appropriate option for the upper boundary of the domain (Figure 3.3).

Tangency is an inviscid, impermeability condition designed for solid wall surfaces which is selected for the body (Figure 3.3).

Axis of Symmetry is the condition applied to the axis of symmetry of the problem configuration (Figure 3.3).

Initial Condition

The time accurate calculation is initialized by the steady state solution of a uniform flow at $M_\infty = 1.89$ past a blunt cylinder in which a bow shock is created ahead of the body. The initial condition is obtained by Gauss–Seidel relaxation using GASPex.

3.4.2 Space Discretization

The selected algorithm for inviscid fluxes is Van Leer’s scheme with third–order upwind biased reconstruction and Min–Mod limiter.

3.4.3 Time Integration

The second order Runge–Kutta method as the time integration scheme in the analysis is employed. The parameter to control is Δt which is selected according two criteria. The time step chosen should resolve the filament motion and also satisfies the stability condition.

The time step is selected so that the filament travels no more than one grid cell within one time step

$$\Delta t \leq \frac{\Delta x}{U_\infty} \quad (3.52)$$

Based on 1–D von Neumann stability analysis for Runge–Kutta scheme, the Courant criterion for the stability of the method is [13]

$$\Delta t \leq \Delta t_{CFL} \quad (3.53)$$

where Δt_{CFL} is defined as

$$\Delta t_{CFL} = \min \frac{\Delta x}{\lambda_m} \quad (3.54)$$

where $\lambda_1 = u$, $\lambda_2 = u + a$, $\lambda_3 = u - a$ and u is the local velocity of the flow.

For this problem Δt_{CFL} can be obtained in both x and y directions

$$\Delta t_{CFLx} = \min \frac{\Delta x}{u_1 + a}$$

$$\Delta t_{CFLy} = \min \frac{\Delta y}{u_2 + a} \quad (3.55)$$

and the smaller of the two (here, Δt_{CFLy}) is taken.

The time step used in these calculations satisfies both equations (3.52) and (3.53).

3.4.4 Post Processing

To investigate the flow structure and also the parameters of our interest such as the amount of drag reduction and efficiency of the process, the primitive flow variables along with the geometric coordinates are written to Tecplot files at specific time intervals. Two other data sets, namely, pressure at the centerline and the pressure along the front body at different instances of time are extracted for further analysis. The data for pressure at the centerline versus time is employed to determine if the flow has reached stochastically stationary behavior. The data for pressure on the front surface versus time is used to compute the percent of drag reduction and energy efficiency of the process.

3.5 Computing Resources

The computations of this study are performed with the local machines that are in the subnet of the Rutgers computer facilities.

In the subnet of Rutgers University, we make use of the following machines throughout this study: tupolev, giovanni and engsoft. The cpu intensive part of the solution of the flow domain is performed on tupolev which is a 12-node Linux cluster with two dual-core processors per node at 2.4 GHz, 1 GByte RAM per processor (24 GByte RAM total), dual 1 Gbit Ethernet, Debian Linux. Giovanni and engsoft are used for grid generation and some post processing applications respectively.

3.6 Validation

The code used as the flow solver has been verified by several cases; however, in this section the steady state solution is taken and two parameters are examined as a validation of GASPEX. Two parameters are chosen, namely, stand-off distance of the shock and the stagnation pressure behind the shock.

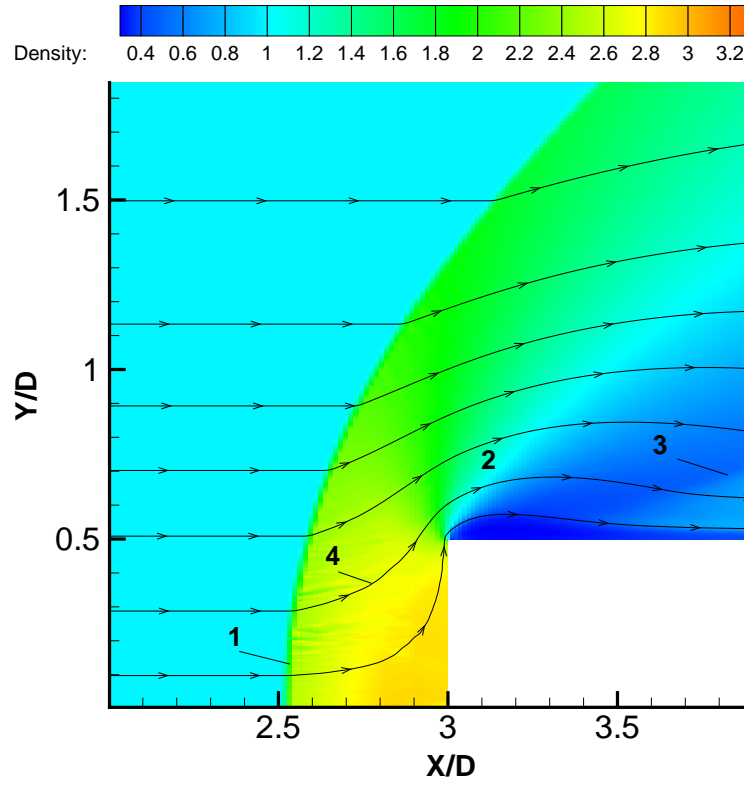


Figure 3.4: The steady state dimensionless density field

As for the first parameter, there have been several articles discussing the stand-off distance of the shock for blunt bodies. For a blunt cylinder in a low supersonic flow, *i.e.*, $M_\infty = 2$, experiments have shown that the stand-off distance of the shock is half of the diameter of the cylinder (see, for example, [19]). The same result is given by our computations and the main features of the flow are specified in Figure 3.4:

1. The bow shock generated ahead of the cylindrical body.
2. The expansion fan formed over the upper corner of the body.
3. The recompression shock formed attached to the body.
4. The flow streamlines.

As for the stagnation point behind the shock, the relations for normal shock are taken and the stagnation pressure is computed based on the conditions in front of the shock and is compared the result with that of the computations. From the normal shock relations [25]

for a perfect gas, the ratio of the stagnation pressure behind the shock to the stagnation pressure ahead the shock is

$$\frac{p_{o2}}{p_{o1}} = \left[1 + \frac{2\gamma}{\gamma + 1}(M_1^2 - 1) \right]^{-1/(\gamma-1)} \left[\frac{(\gamma + 1)M_1^2}{(\gamma - 1)M_1^2 + 2} \right]^{\gamma/(\gamma-1)} \quad (3.56)$$

Substituting for $M_1 = M_\infty = 1.89$ and $\gamma = 1.4$, one obtains

$$p_{o2} = p_{o1}/1.2954 \quad (3.57)$$

The dimensionless stagnation pressure ahead the shock is $p_{o1} = 1.3194$. Using the ratio from equation (3.57), $p_{o2} = 1.0100$. The stagnation pressure behind the shock is $p_{o2} = 1.0149$ from the GASPex calculations, therefore

$$\frac{(p_{o2})_{GASPex} - (p_{o2})_{normalshock}}{(p_{o2})_{normalshock}} = 0.005$$

where $(p_{o2})_{GASPex}$ denotes the stagnation pressure given by the flow solver's calculations and $(p_{o2})_{normalshock}$ denotes the stagnation pressure obtained from normal shock relations. This indicates that the accuracy of our computed results is within the range of the accuracy with which the stagnation pressure is measured in supersonic speeds and therefore, the computations are done with enough accuracy.

Chapter 4

Results

In this work, the effect of altering the frequency of the pulses on the flow structure is examined. Furthermore, determining the amount of front drag reduction on the body using the periodic pulses of MW filaments is of interest. Also, as a measure of the efficiency of the process, the energy efficiency as a function of the frequency of the pulses is studied. To do this, four different cases are studied. The freestream Mach number is $M_\infty = 1.89$ and the degree of rarefaction is $\alpha = 0.5$ for all cases, and $\gamma = 1.4$. A summary of the problems examined is presented in Table 4.1. Case 1 considers an infinitely long filament with the diameter of $d/D = 0.1$. Cases 2–4 examine the effect of multiple filaments of the same diameter but with different frequencies.

This chapter is started with a section presenting the steady state case to compare with the unsteady flow as a result of the interaction of filament(s) with the shock layer. A study of flow structure and the efficiency for each case is done separately in the following sections.

4.1 Numerical Results for Different Cases

In this section, the results of numerical modeling using GASPex are provided for the case of steady-state and all four cases summarized in Table 4.1. Three sets of results for the unsteady cases are presented. The first set is to show the achievement of stochastically

Case	Description	$\frac{d}{D}$	$\frac{l}{D}$	$\frac{L}{D}$
1	Infinitely long filament	0.10	∞	n/a
2	Finite multiple filaments	0.10	1.0	4/3
3	Finite multiple filaments	0.10	1.0	2
4	Finite multiple filaments	0.10	1.0	4

Table 4.1: Studied Cases

stationary behavior of the flow. The second set demonstrates the visualization of the flow field by pressure and density contours along with the numerical Schlieren images. Finally, the last set describes the efficiency of the energy deposition in reducing drag for each case.

4.1.1 Steady State

When a supersonic uniform flow pasts a blunt cylinder, a bow shock is formed ahead of the body with a stand-off distance. The density contour (ρ/ρ_∞) is chosen to represent the flow field in this case (Figure 4.1). The stand-off distance equals to $D/2$ which is in agreement with the experiment [19]. Although the study of steady state condition is not the principal interest of this work, the case is presented to compare with the unsteady behavior.

The main regions of the flow formed in a uniform supersonic ($M_\infty = 1.89$) flow in the vicinity of a cylindrical body are specified in Figure 4.1:

1. The bow shock generated ahead of the cylindrical body.
2. The expansion fan formed over the upper corner of the body.
3. The recompression shock formed attached to the body.
4. The flow streamlines.

4.1.2 Stochastically Stationary State

The nature of our problem is an unsteady behavior with a natural frequency associated with it. Having said that, however, one does not observe a periodic behavior in a sense that everything repeats exactly during the development of the flow. Eventually, a stochastically stationary state should be achieved. To examine whether or not the flow has reached its stochastically stationary state, the evolution of two different quantities, namely the mean pressure and the pressure fluctuations at the centerline are investigated. The mean pressure is formulated as follows

$$p_{mean}(n) = \frac{\int_{t_i}^{t_n} p_{centerline}(t) dt}{t_n - t_i} \quad (4.1)$$

where $p_{mean}(n)$ is the mean pressure corresponding to the n^{th} interaction, t_i indicates the time of first interaction and t_n is the time required for the n^{th} interaction. Equation (4.1) is then nondimensionalized appropriately (see Section 3.1.1) and is plotted versus the number of pulses interacted with the shock layer.

The pressure fluctuations is formulated as follows

$$p_{fluc.}(n) = \frac{\int_{t_i}^{t_n} (p_{centerline}(t) - p_{mean}(n))^2 dt}{t_n - t_i} \quad (4.2)$$

where $p_{fluc.}(n)$ is the pressure fluctuations corresponding to the n^{th} interaction. Equation (4.2) is then nondimensionalized appropriately and is plotted versus the number of pulses interacted with the shock layer.

The trend of mean pressure and pressure fluctuations at the centerline is examined, where pressure is nondimensionalized by $\rho_\infty U_\infty^2$. The stochastically stationary state is determined when both quantities (averaged mean pressure and averaged pressure fluctuations) converge to constant values. Further analysis is carried out on the flow by examining a period of time after the stochastically stationary behavior is obtained.

The corresponding plots for each case are presented in Figures 4.2 to 4.5. For the case of an infinitely long filament, this state is achieved approximately at a dimensionless time ($t^* = t/(D/U_\infty)$) equal to 70, whereas for the case, $L/D = 4$, it takes a dimensionless time equal to 18 for the flow to reach stochastically stationary behavior. This might be associated with the fact that as the period of each pulse increases, the time between two successive pulses increases as well and the flow has more time to retain its previous state between two interactions.

4.1.3 Visualization of Flow

Case 1 : Infinitely Long Filament

Case	Description	$\frac{d}{D}$	$\frac{l}{D}$	$\frac{L}{D}$
1	Infinitely long filament	0.10	∞	n/a

Table 4.2: Case 1

The interaction of an infinitely long filament with the shock layer ahead of a blunt cylinder is studied. The evolution of the flow is demonstrated by the density (ρ/ρ_∞) and pressure field ($p/\rho_\infty U_\infty^2$) along with numerical Schlieren images (Figures 4.6–4.8). Since there is no natural period associated with the case of an infinitely long filament, the behavior of the flow is chosen to be investigated over a dimensionless time duration equal to 1.03.

The beginning of the interaction process causes the bow shock wave motion from the body and generation of a contact discontinuity instability similar to the Richtmeyer-Meshkov instability (see, Meshkov [28]). A significant increase (typically twice as much) in stand-off distance is observed compared to the steady-state case (Figure 4.1). The reason of the instability generation is an impulse effect of the bow shock wave upon the contact discontinuities (horizontal and vertical) representing the boundaries of the heated channel.

This instability generates a toroidal vortex. It is seen that a triple point configuration is formed at the bow shock front fracture (Figure 4.8). The vortex structure generated from the rolled contact boundaries reaches the body and consequently decreases the pressure on it. Near the front surface of the body, the reversed circulation flow is formed (Figure 4.6) and later it stops the boundary of the heated area. Eddies generated stochastically as the result of the shear layer instability move towards the upper corner of the body and interact with the body causing a series of weak shock waves towards the bow wave and a series of shock waves normal to the front body's surface (Figures 4.7 and 4.8).

Main regions of flow are seen in Figures 4.6 to 4.8¹:

1. The low-density infinite filament.
2. The bow shock formed ahead of the cylindrical body.
3. The expansion fan formed over the corner of the cylindrical body.
4. The recompression shocks formed attached to the body.
5. The normal shocks generated at the front body's surface.
6. The lensing effect caused by the interaction of the filament with the shock layer.

¹The weak wave upstream the bow shock is a numerical phenomenon associated with the discontinuity across the boundary of the filament. This is a benign feature and has no effect on the flow structure.

7. The vortex generation within the shock layer during the interaction.
8. The contact discontinuity formed where two flows of different density and temperature meet.
9. The weak shocks formed within the shock layer moving towards the bow shock.

Case 2: Finite Multiple Filaments ($L/D = 4/3$)

Case	Description	$\frac{d}{D}$	$\frac{l}{D}$	$\frac{L}{D}$
2	Finite multiple filaments	0.10	1.0	4/3

Table 4.3: Case 2

The results presented in this section is the first in the series of studying the interaction of a train of finite periodic pulses with the shock layer. The computations are run for an effectively infinite number of pulses. Dimensionless density contours (nondimensionalized by ρ/ρ_∞) along with instantaneous streamlines, pressure contours ($p/\rho_\infty U_\infty^2$) and numerical Schlieren images are chosen to represent the flow field during one pulse period at different instants of time where time is nondimensionalized by D/U_∞ (Figures 4.9 to 4.11). The main features of the flow are the same as the case of an infinitely long filament; however, the general effect such as the increase in stand-off distance is weaker in the current case. Four basic features of the flow are observed during the interaction:

1. When the filament reaches the shock layer, it modifies the shape of the bow shock. As a result, the shock lenses forward. This behavior has been previously observed (see, for example, Georgievskii and Levin [10]).
2. A toroidal vortex region is generated (see, for example, Azarova and Kolesnichenko [3]).
3. A stagnation point is formed and an effective momentary aerodynamic streamlining of the body results.
4. As the filament penetrates into the shock layer, the vortex region convects past the cylinder and eventually leaves the flow domain.

During the interaction, main regions of the flow are formed which are specified in Figures 4.9 to 4.11

1. The low-density finite filament.
2. The bow shock formed ahead of the cylindrical body.
3. The expansion fan formed over the corner of the cylindrical body.
4. The recompression shock formed at the body.
5. The weak shocks normal to the front surface of the body.
6. The weak shocks formed within the shock layer.
7. The lensing effect caused by the interaction of the filament with the shock layer.
8. The vortex generation within the shock layer during the interaction.
9. The contact discontinuity formed where two flows of different density and temperature meet.

Case 3 : Finite Multiple Filaments ($L/D = 2$)

Case	Description	$\frac{d}{D}$	$\frac{l}{D}$	$\frac{L}{D}$
3	Finite multiple filaments	0.10	1.0	2

Table 4.4: Case 3

In this section, the interaction of an effectively infinite number of periodic pulses ($L/D = 2$) with the cylindrical shock layer is considered to examine the flow structure during the interaction. The unsteady behavior of the flow is shown in Figures 4.12– 4.14 at different instants of time where time is nondimensionalized by D/U_∞ . Density contours (ρ/ρ_∞), pressure contours ($p/\rho_\infty U_\infty^2$) and numerical Schlieren images are shown together with instantaneous streamlines. All the figures correspond to one pulse period (*i.e.*, L/D). It should be noted that the increase in the stand-off distance is less compared to the case of an infinitely long filament. Also, the bow shock is flatter compared to the infinitely long filament case (Figure 4.6). Four basic phenomena are observed during the interaction:

1. When the filament reaches the shock layer, it modifies the shape of the bow shock. As a result, the shock lenses forward. This behavior has been previously observed (see, for example, Georgievskii and Levin [10]).
2. A toroidal vortex region is generated (see, for example, Azarova and Kolesnichenko [3]).
3. A stagnation point is formed and an effective momentary aerodynamic streamlining of the body results.
4. As the filament penetrates into the shock layer, the vortex region convects past the cylinder and eventually leaves the flow domain.

During the interaction, main regions of the flow are formed which are specified in Figures 4.12 to 4.14

1. The low-density finite filament.
2. The bow shock formed ahead of the cylindrical body.
3. The expansion fan formed over the corner of the cylindrical body.
4. The recompression shock formed at the body.
5. The weak shocks normal to the front surface of the body.
6. The weak shocks formed within the shock layer.
7. The lensing effect caused by the interaction of the filament with the shock layer.
8. The vortex generation within the shock layer during the interaction.
9. The contact discontinuity formed where two flows of different density and temperature meet.

Case 4 : Finite Multiple Filaments ($L/D = 4$)

In this section, the interaction of an effectively infinite number of periodic pulses with the same size as the previous case but with different duration ($L/D = 4$) with the shock layer is examined. Similar to the previous case, contours of density (ρ/ρ_∞), pressure ($p/\rho_\infty U_\infty^2$) and

Case	Description	$\frac{d}{D}$	$\frac{l}{D}$	$\frac{L}{D}$
4	Finite multiple filaments	0.10	1.0	4

Table 4.5: Case 4

numerical Schlieren images are chosen to represent the flow together with instantaneous streamlines (Figures 4.15 – 4.17). The same as before, four basic flow structures are of interest. A modification in the shape of bow shock (lensing effect) is observed, however, the increase in stand-off distance is even less in the current case compared to the cases 1 and 3.

Similar to the previous case, different regions of flow are specified in Figures 4.15 to 4.17:

1. The low-density finite filament.
2. The bow shock formed ahead of the cylindrical body.
3. The expansion fan formed over the corner of the cylindrical body.
4. The recompression shocks formed attached to the body.
5. The lensing effect caused by the interaction of the filament with the shock layer.
6. The vortex generation within the shock layer during the interaction.
7. The contact discontinuity formed where two flows of different density and temperature meet.
8. The weak shocks formed within the shock layer.

4.1.4 Drag Reduction Effectiveness and Efficiency

In this section, the drag reduction effectiveness and efficiency of the process of the interaction of the MW filament(s) with the cylindrical shock layer for each case are studied. A detailed description of the formulation of effectiveness and efficiency is presented followed by the results of them in each case.

Formulation

The effectiveness, ζ , is a measure of the drag reduction and is defined as the ratio of the average drag savings during the interaction of one MW filament with the shock layer to the drag in the absence of the MW filament

$$\zeta = \frac{\int_0^{L/D} \int_0^{1/2} (p_o - p) r dr dt}{\frac{L}{D} \int_0^{1/2} p_o r dr} \quad (4.3)$$

Equation (4.3) is in nondimensional form and p_o and p are front pressure in the absence and in the presence of the MW filament respectively.

For the case of infinitely long filament, since there is no natural frequency present in the problem, τ_∞ is defined as the time of computation. The nondimensional effectiveness is therefore as follows

$$\zeta = \frac{\int_0^{\tau_\infty} \int_0^{1/2} (p_o - p) r dr dt}{\tau_\infty \int_0^{1/2} p_o r dr} \quad (4.4)$$

The efficiency is defined as the ratio of energy saved during the interaction of one MW filament with the shock layer to the energy consumed to create that filament. Assume for simplicity that the energy deposition occurs at constant pressure (isobaric) and in a cylindrical region of diameter d ("filament") and streamwise length of l aligned with the flow and initially located upstream of the blunt body. The net energy ΔE_f added in volume $A_\infty l$ to increase the temperature from the ambient T_∞ to the level $T_f = T_\infty + \Delta T$ is [14]

$$\Delta E_f = A_\infty l c_p \rho_f \Delta T \quad (4.5)$$

where ρ_f is the density of the filament. Since the energy is assumed added at constant pressure,

$$\Delta E_f = A_\infty l c_p \frac{p_\infty}{R} (1 - \alpha) \quad (4.6)$$

where R is the gas constant for air and α is the ratio of the density of the filament to the freestream density. Hence, the expression for energy efficiency is

$$\eta = \frac{\int_o^\tau (U_\infty \int_A p_o dA - U_\infty \int_A p dA) dt}{(\pi \frac{d^2}{4} l) (c_p \frac{p_\infty}{R}) (1 - \alpha)} \quad (4.7)$$

where $\tau = L/U_\infty$ is the duration of one MW pulse, p_o and p are front pressure in the absence and in the presence of the MW filament respectively and A is the front area of the body.

Using the same reference parameters used to find the dimensionless parameters associated with the problem, the formulation for η in dimensionless form is obtained

$$\eta = \frac{8(\gamma - 1)M_\infty^2}{(1 - \alpha)} \left(\frac{D}{d}\right)^2 \left(\frac{D}{l}\right) \int_o^{L/D} \int_o^{1/2} (p_o^* - p^*) r^* dr^* dt^* \quad (4.8)$$

The dimensionless are parameters as follows

$$\begin{aligned} \gamma &= 1.4 \\ \alpha &= 0.5 \\ M_\infty &= 1.89 \\ \frac{d}{D} &= 0.1 \\ \frac{l}{D} &= 1.0 \end{aligned}$$

Thus, the final dimensionless relation used to calculate the efficiency η is (for simplicity, * is dropped):

$$\eta = 2.286 \times 10^3 \int_o^{L/D} \int_o^{1/2} (p_o - p) r dr dt \quad (4.9)$$

For the case of infinitely long filament, since there is no natural frequency present in the problem, τ_∞ is defined as the time of computation. Similar to the case of finite filament with appropriate nondimensionalization, one obtains

$$\eta = \frac{8(\gamma - 1)M_\infty^2}{(1 - \alpha)} \left(\frac{D}{d}\right)^2 \frac{1}{\tau_\infty} \int_o^{\tau_\infty} \int_o^{1/2} (p - p_o) r dr dt \quad (4.10)$$

Results

The results for the effectiveness of the process of the interaction of the MW filament(s) with the shock layer are presented in Figure 4.18. As it is clear in the figures, the maximum effectiveness is that of the case of an infinitely long filament and as the period of the pulses increases in the cases 2 to 4, the percent of drag reduction drops.

The drag reduction efficiency is calculated based on equation (4.10) for the case of infinitely long filament and equation (4.9) for the train of finite filaments. Then the averaged amount over time is plotted versus the number of pulses interacting with the shock layer. As it can be seen in Figure 4.19, the maximum efficiency is that of the case of $L/D = 4$ among these four cases; however, by comparing the amount of drag reduction for cases 1 to 4 (see, Figure 4.18), one concludes that in spite of an increase in drag efficiency in case 4, the amount of drag reduction decreases compared to other cases and the increase in efficiency is due to the small value of energy added to create the MW pulse. It is again clear from the results that the amount of efficiency do not differ that much for the case of $L/D = 4/3$ compared with the infinitely long filament case which is an interesting result, since it is not possible to maintain an infinitely long filament in practice. These results regarding the energy effectiveness and efficiency are summarized in Figures 4.20 and 4.21 where the asymptotic values of the drag reduction effectiveness and efficiency for cases 2–4 are plotted. The efficiency associated with the infinitely long case is specified in the figures as well.

Figure 4.22 demonstrates the Pareto sets of non-dominated configurations (cases 1, 2 and 4) considering the drag reduction effectiveness and efficiency together in which the maximum of efficiency is achieved in the case of $L/D = 4/3$ with the minimum effectiveness associated with it. On the other hand, as it can be seen in Figure 4.22, the maximum effectiveness is that of the infinitely long filament but the efficiency is not maximum in this case.

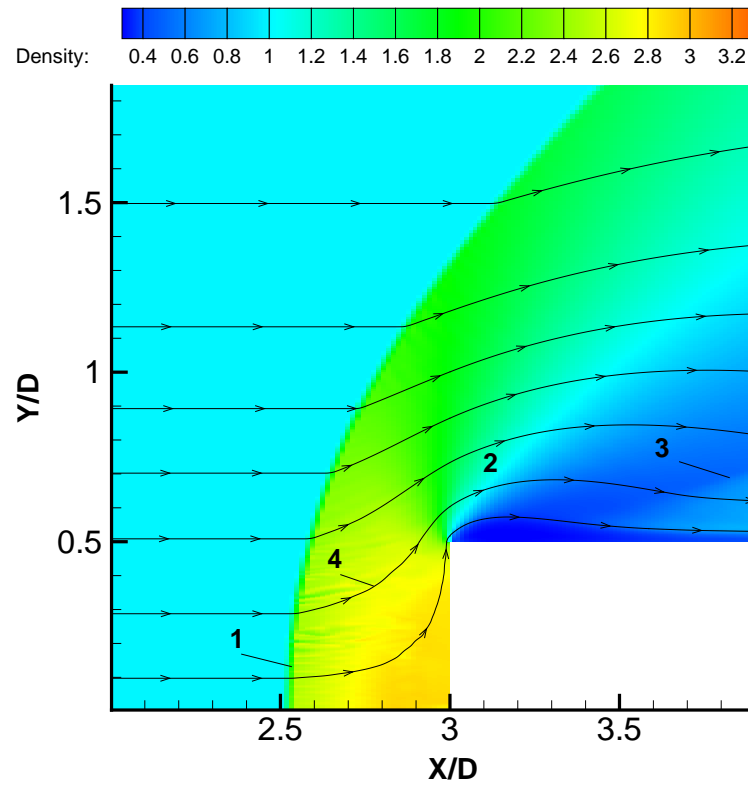


Figure 4.1: The steady state density field

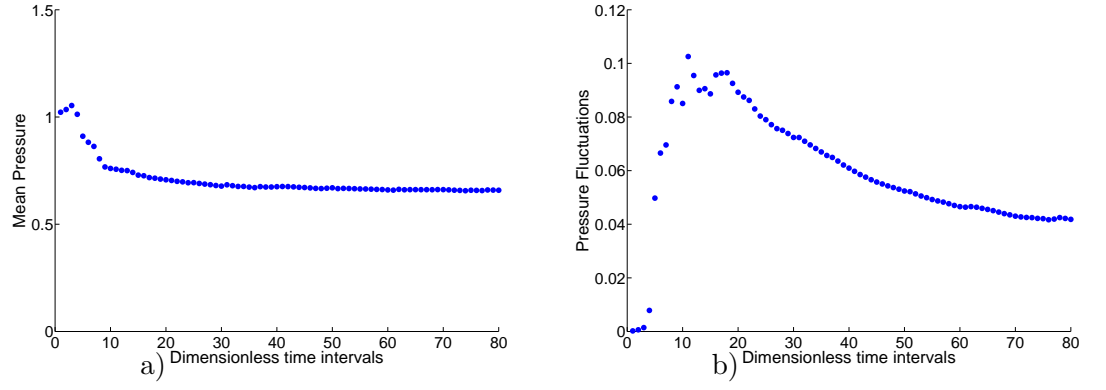


Figure 4.2: Infinitely long filament a) Mean pressure at the centerline, b) Pressure fluctuations at the centerline

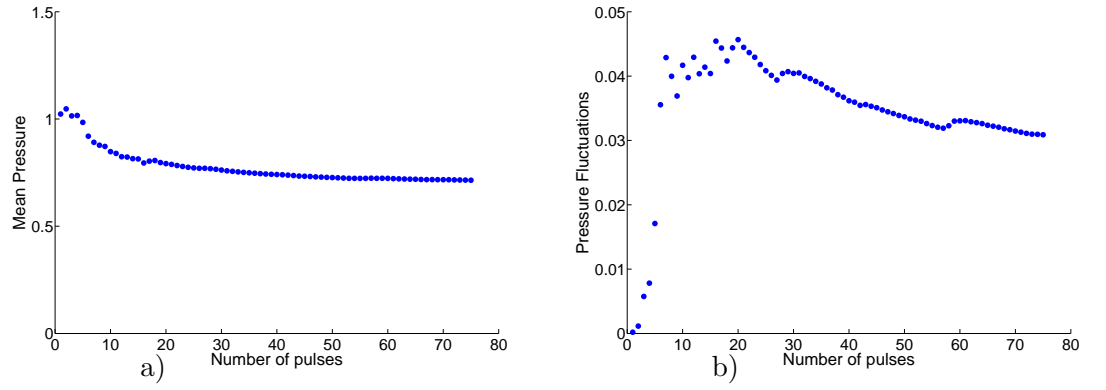


Figure 4.3: $L/D = 4/3$, a) Mean pressure at the centerline, b) Pressure fluctuations at the centerline

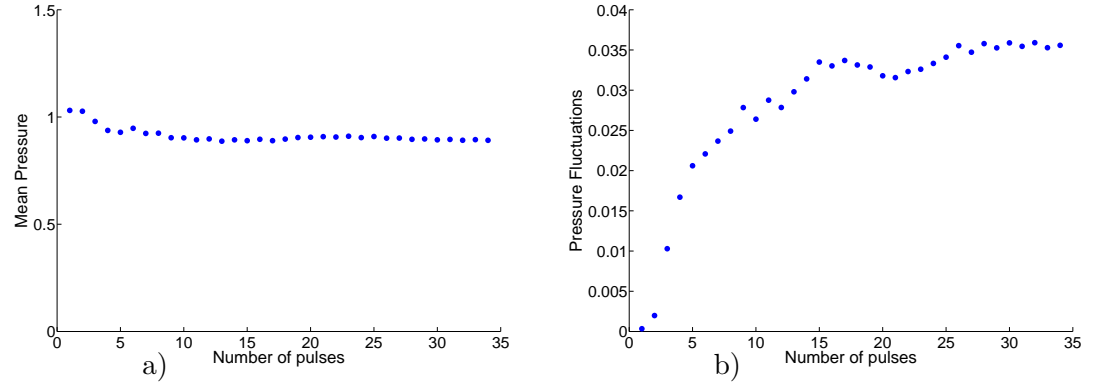


Figure 4.4: $L/D = 2$, a) Mean pressure at the centerline, b) Pressure fluctuations at the centerline

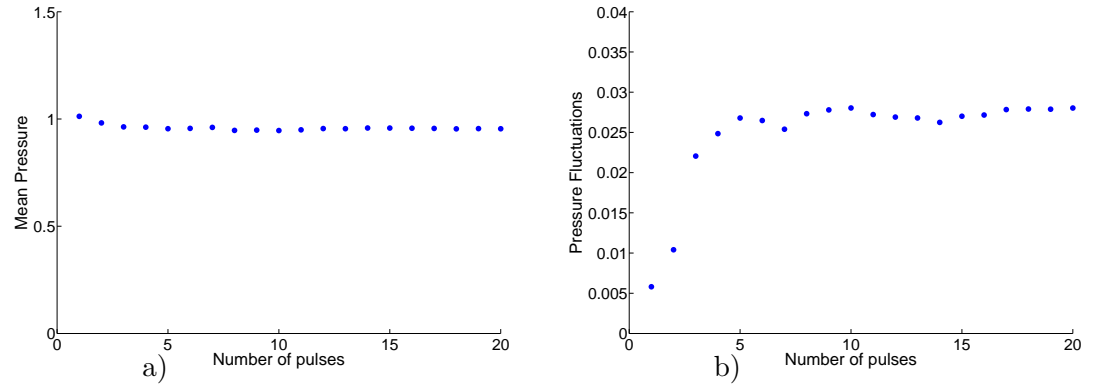


Figure 4.5: $L/D = 4$, a) Mean pressure at the centerline, b) Pressure fluctuations at the centerline

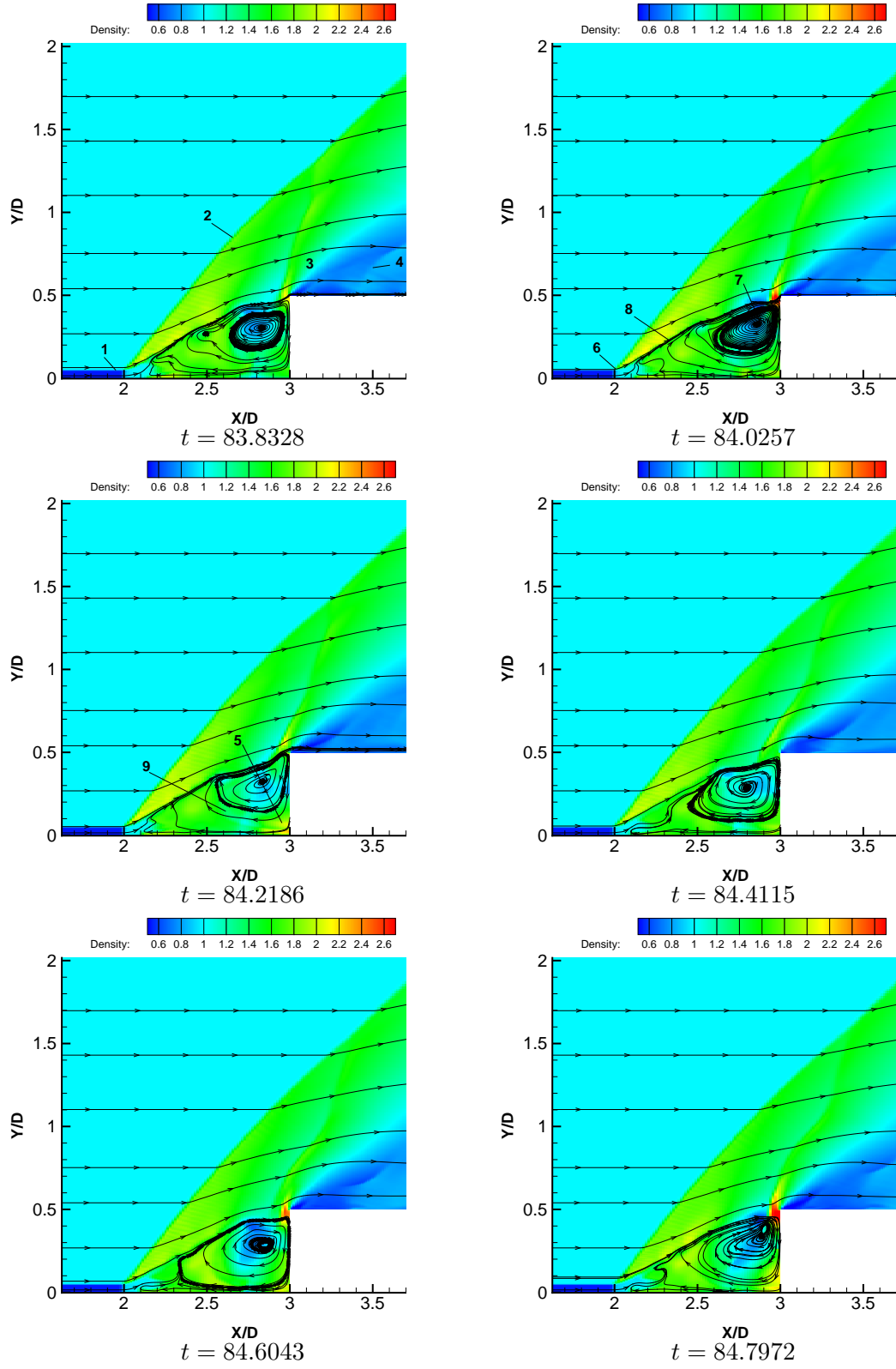


Figure 4.6: The density field for the interaction of infinitely long filament with the shock layer

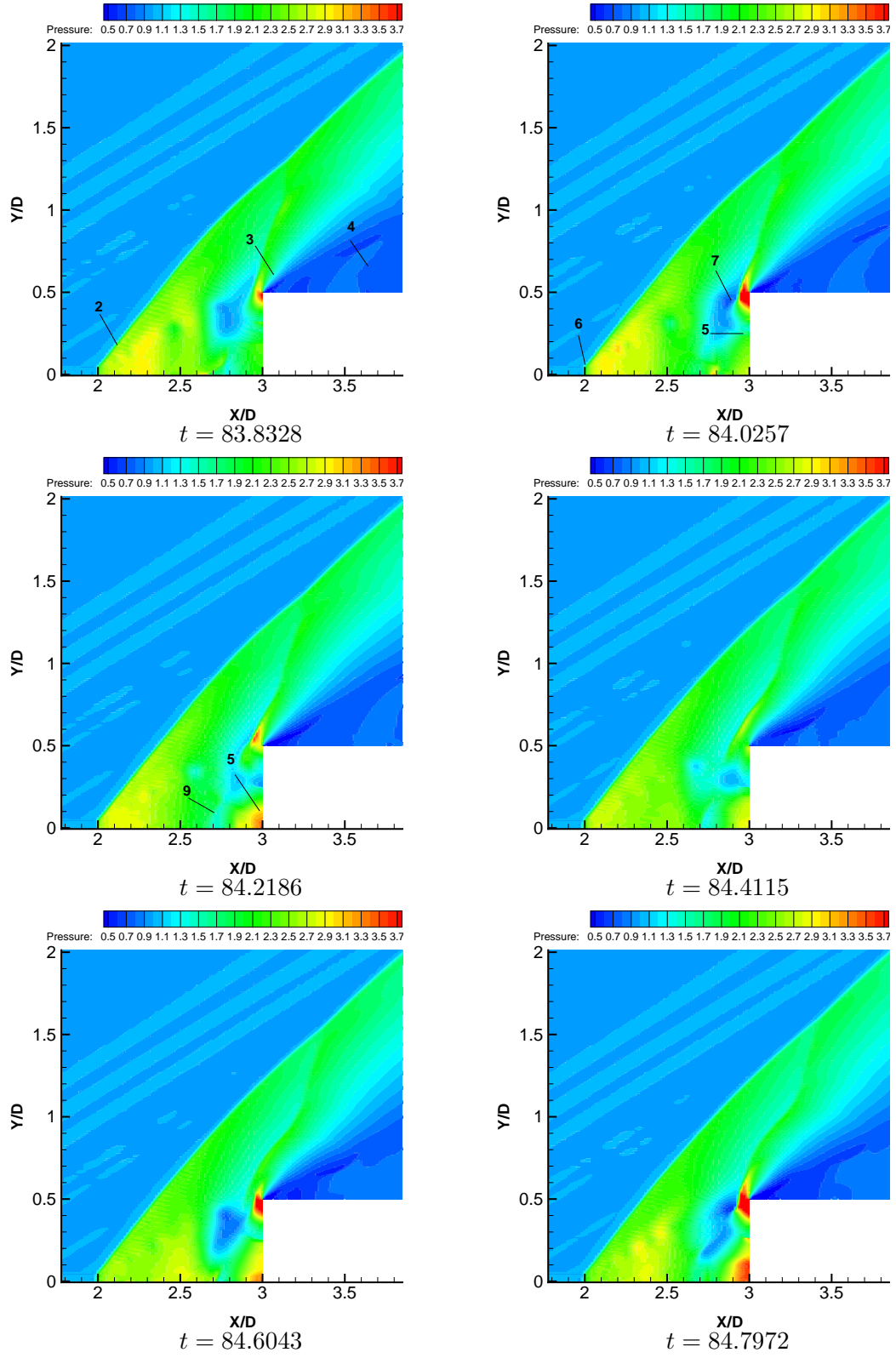


Figure 4.7: The pressure field for the interaction of infinitely long filament with the shock layer

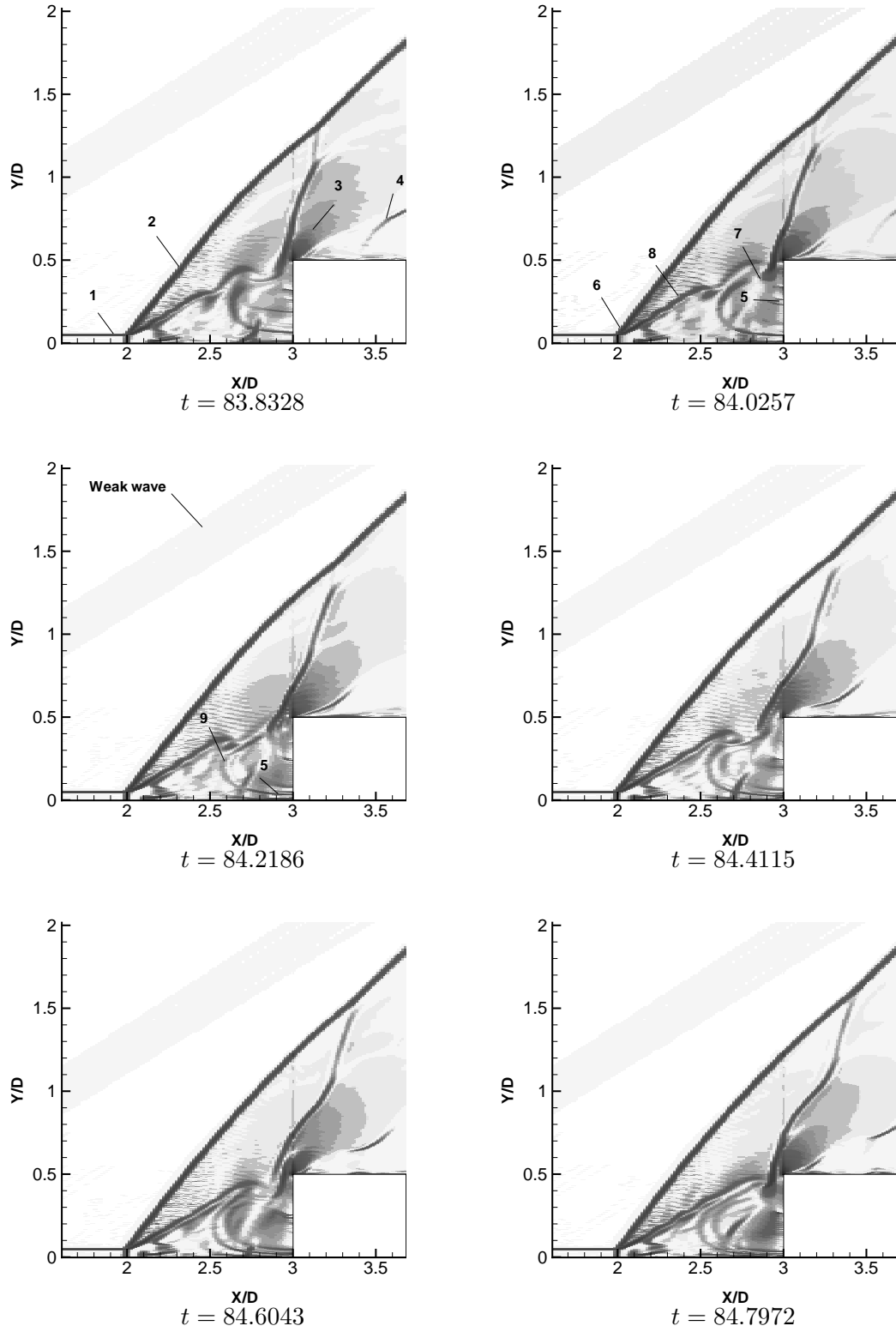


Figure 4.8: Numerical Schlieren images for the interaction of infinitely long filament with the shock layer

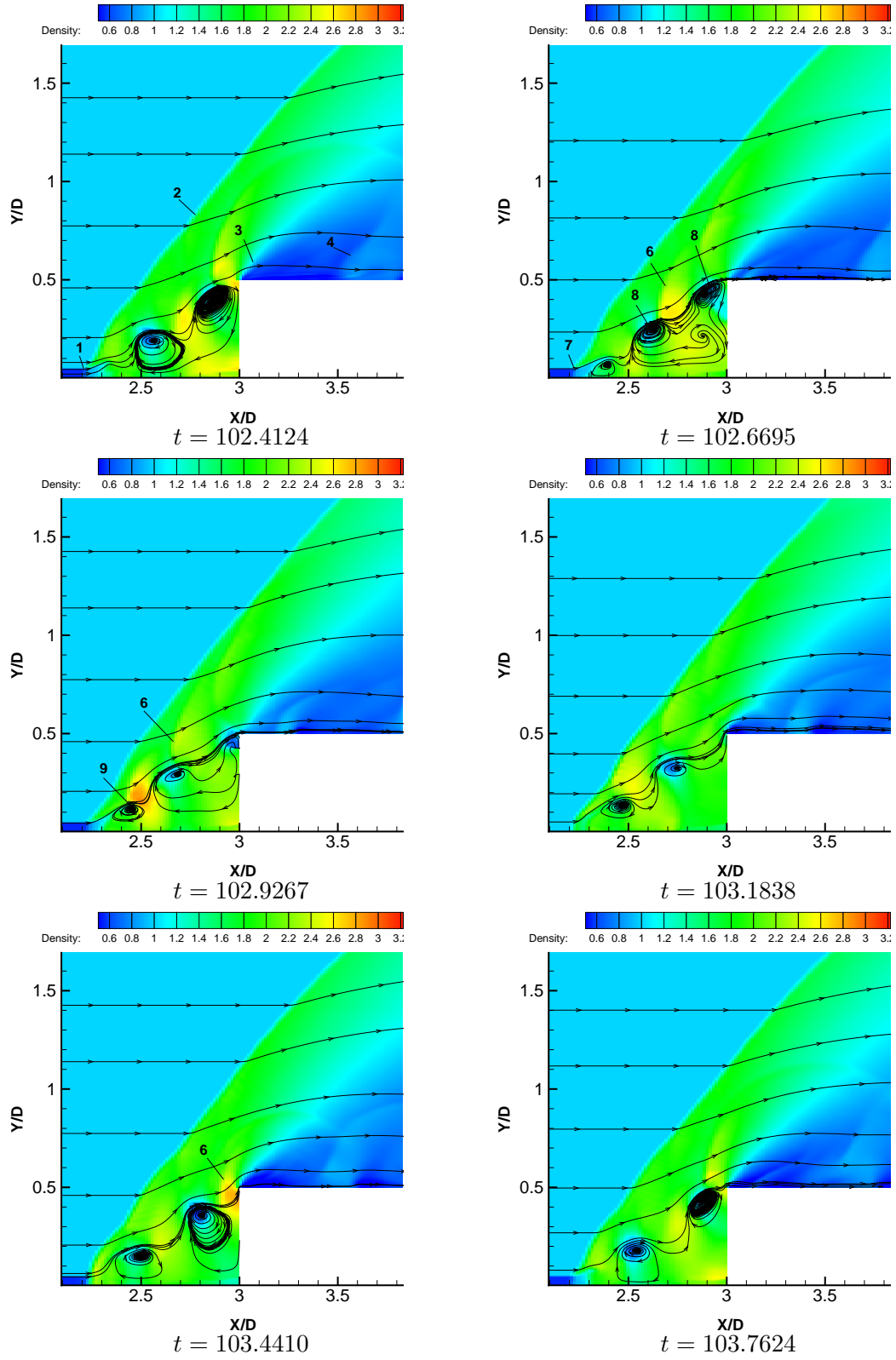


Figure 4.9: The density field for the interaction of the train of finite filaments with the shock layer ($L/D = 4/3$)

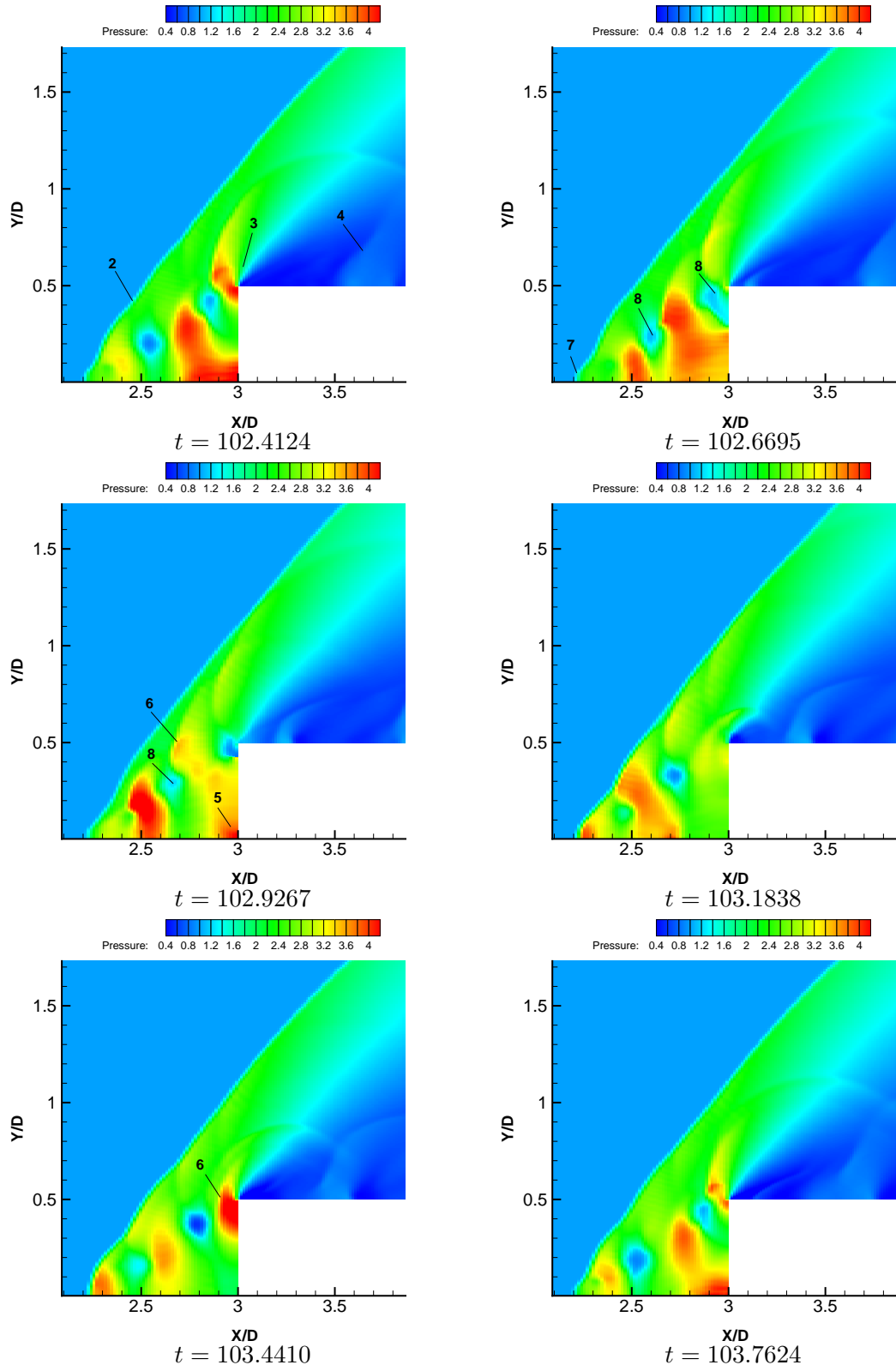


Figure 4.10: The pressure field for the interaction of the train of finite filaments with the shock layer ($L/D = 4/3$)

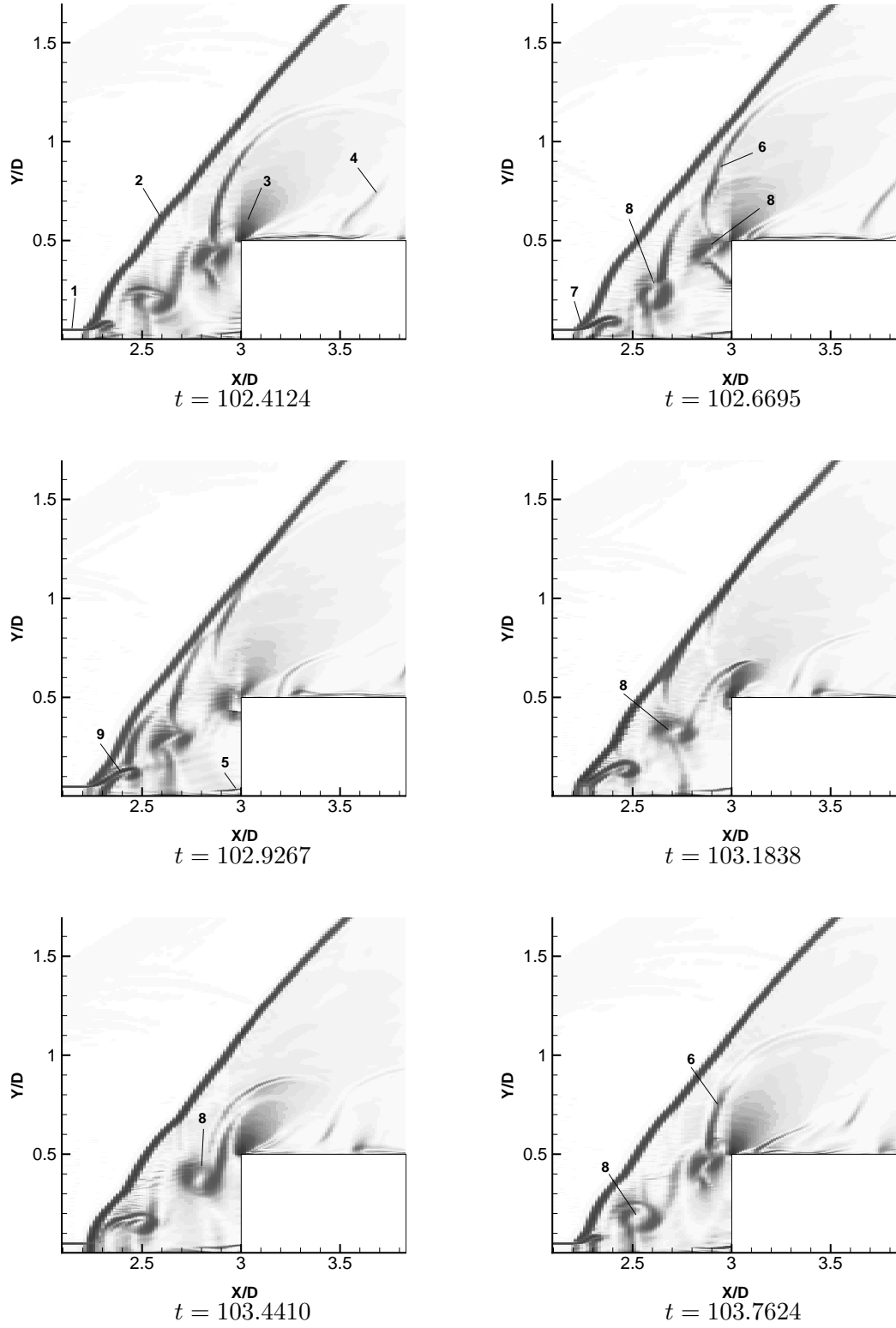


Figure 4.11: Numerical Schlieren image for the interaction of the train of finite filaments with the shock layer ($L/D = 4/3$)

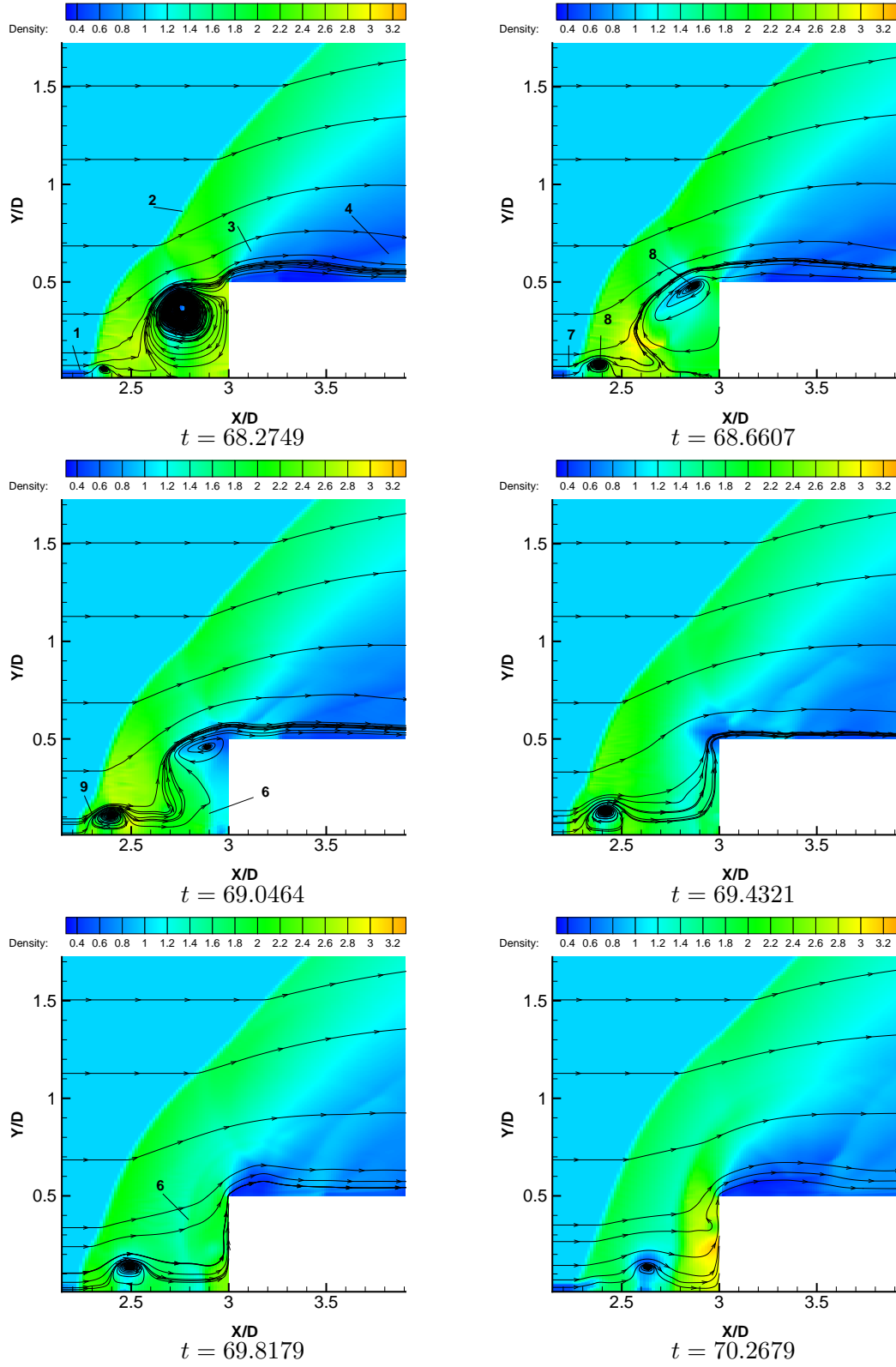


Figure 4.12: The density field for the interaction of the train of finite filaments with the shock layer ($L/D = 2$)

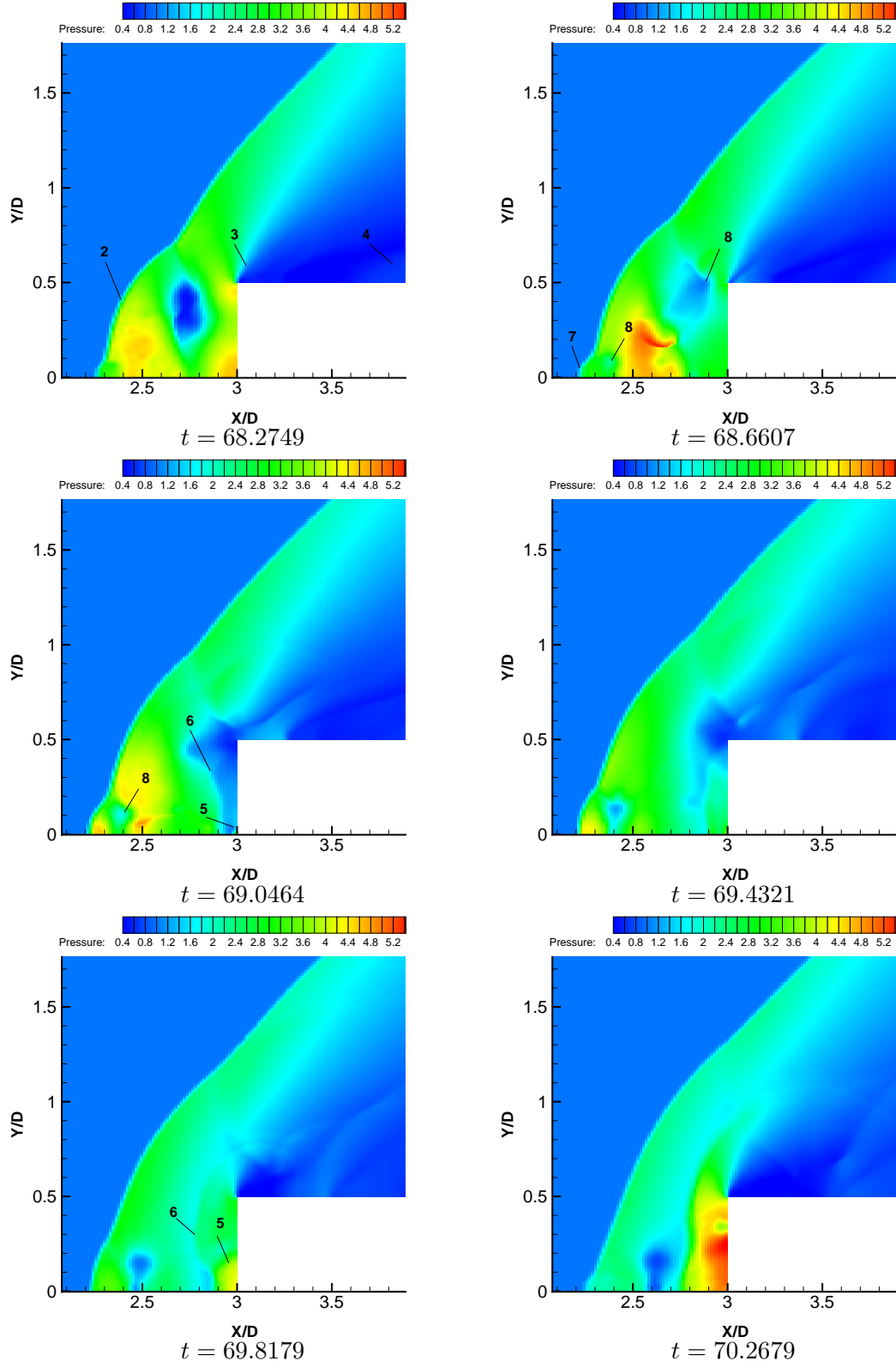


Figure 4.13: The pressure field for the interaction of the train of finite filaments with the shock layer($L/D = 2$)

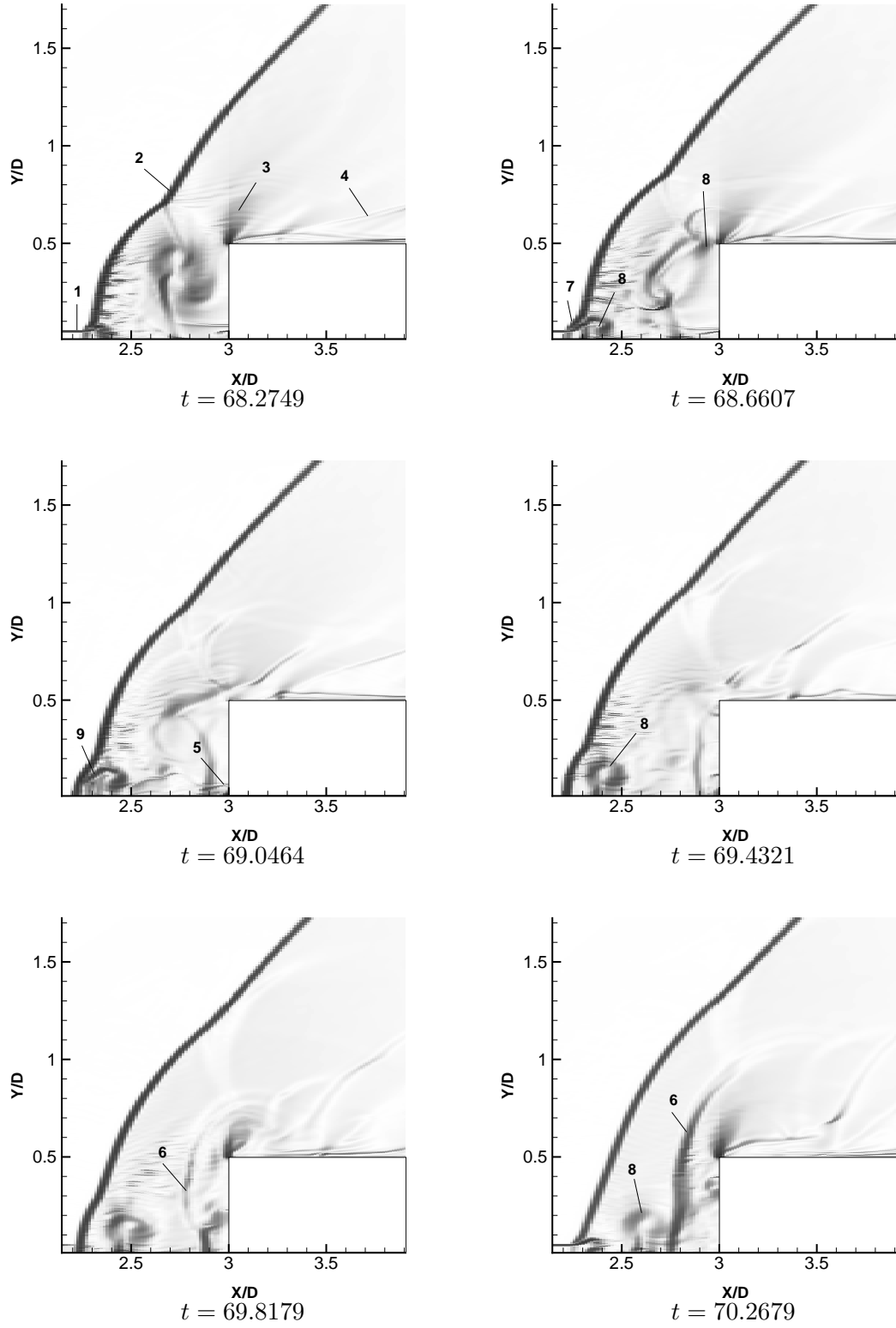


Figure 4.14: Numerical Schlieren image for the interaction of the train of finite filaments with the shock layer ($L/D = 2$)

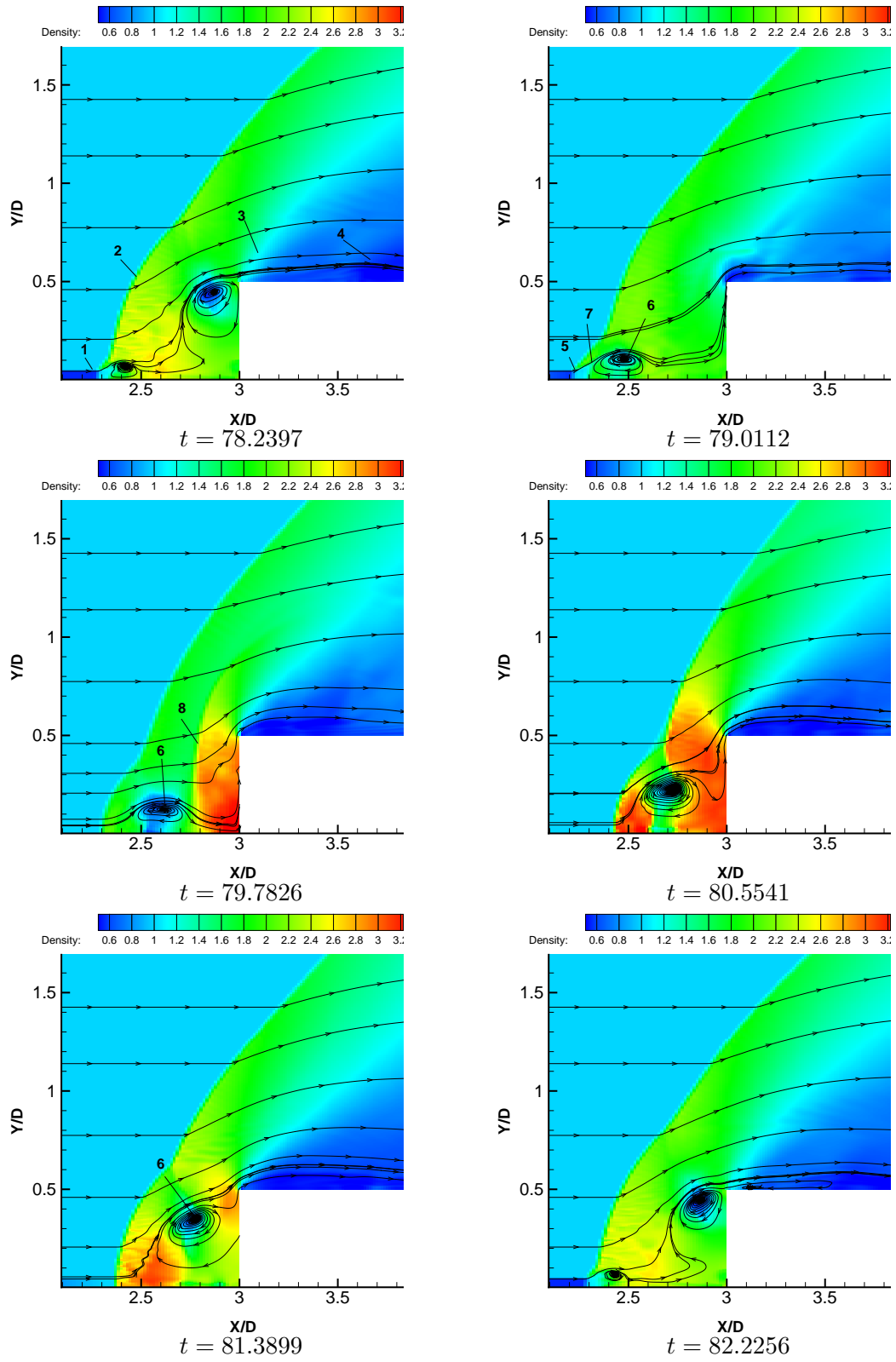


Figure 4.15: The density field for the interaction of the train of finite filaments with the shock layer ($L/D = 4$)

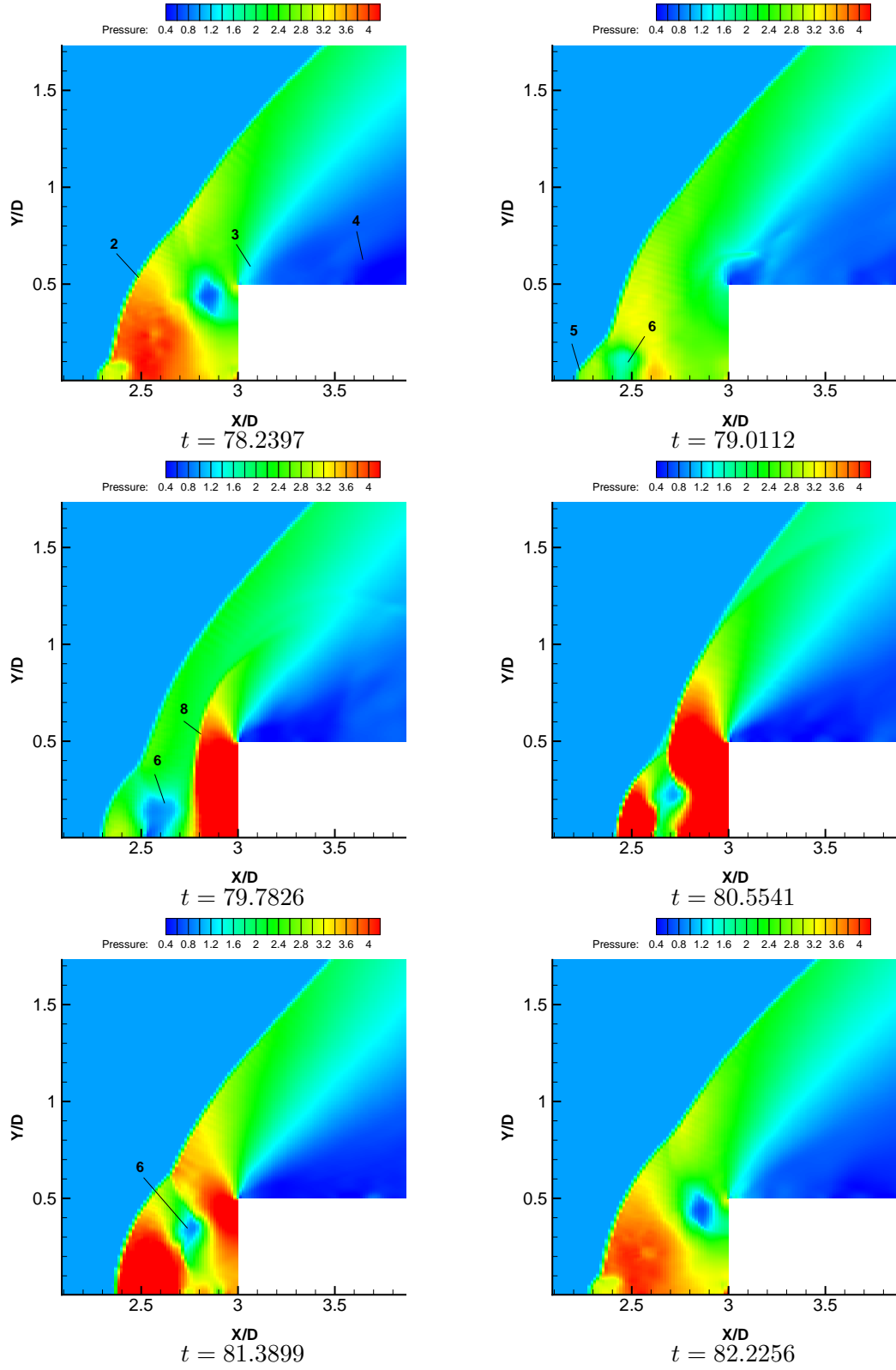


Figure 4.16: The pressure field for the interaction of the train of finite filaments with the shock layer($L/D = 4$)

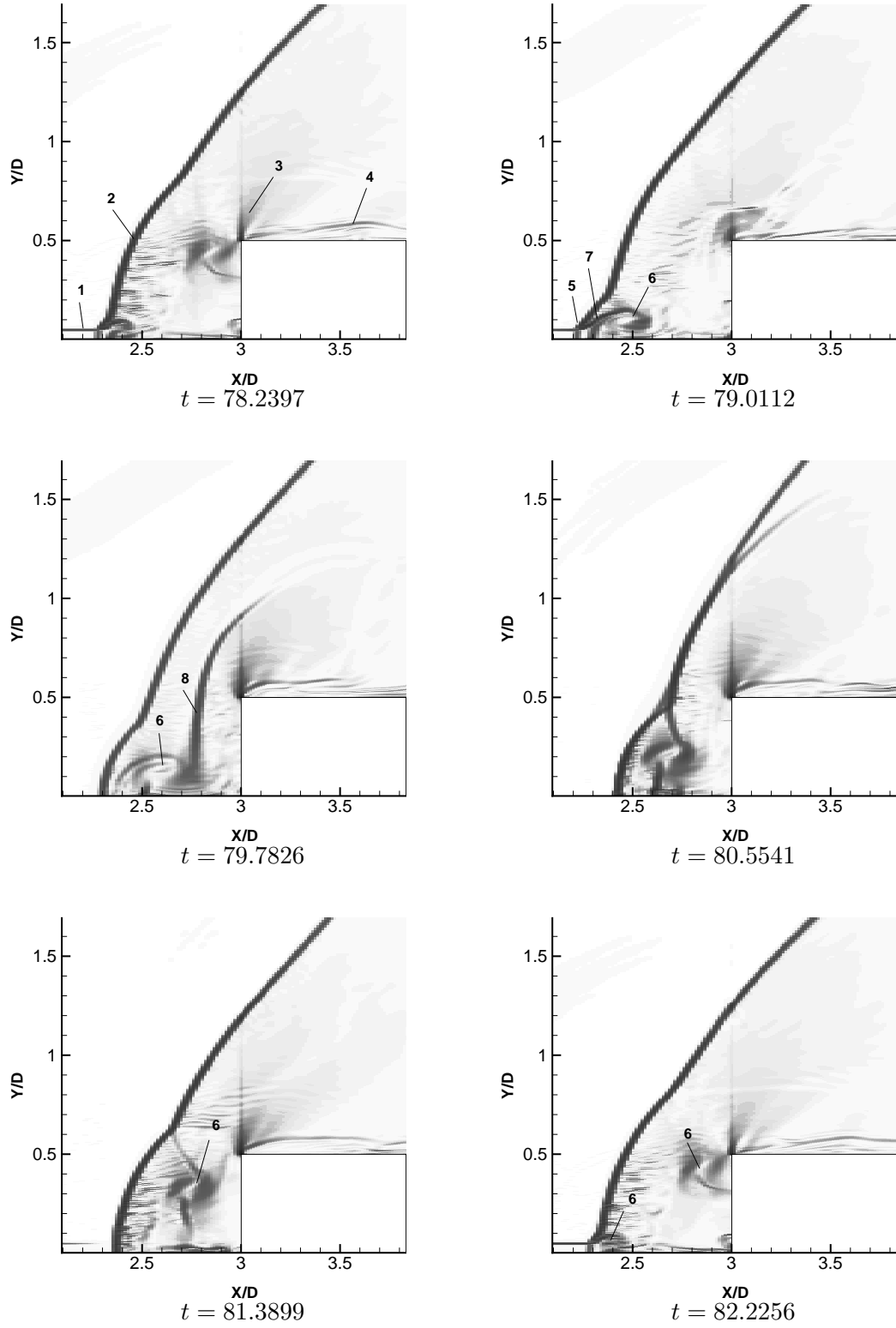


Figure 4.17: Numerical Schlieren image for the interaction of the train of finite filaments with the shock layer ($L/D = 4$)

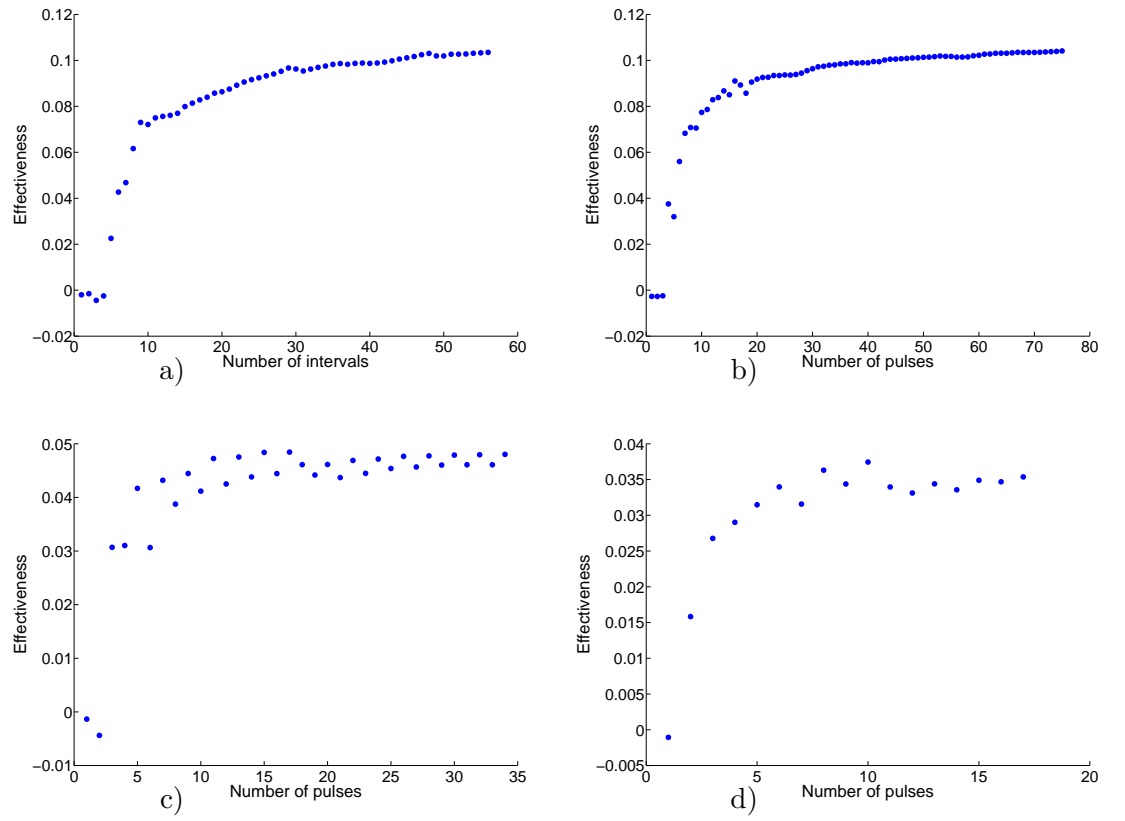


Figure 4.18: The amount of drag reduction for: a) infinitely long filament b) $L/D = 4/3$
c) $L/D = 2$ d) $L/D = 4$

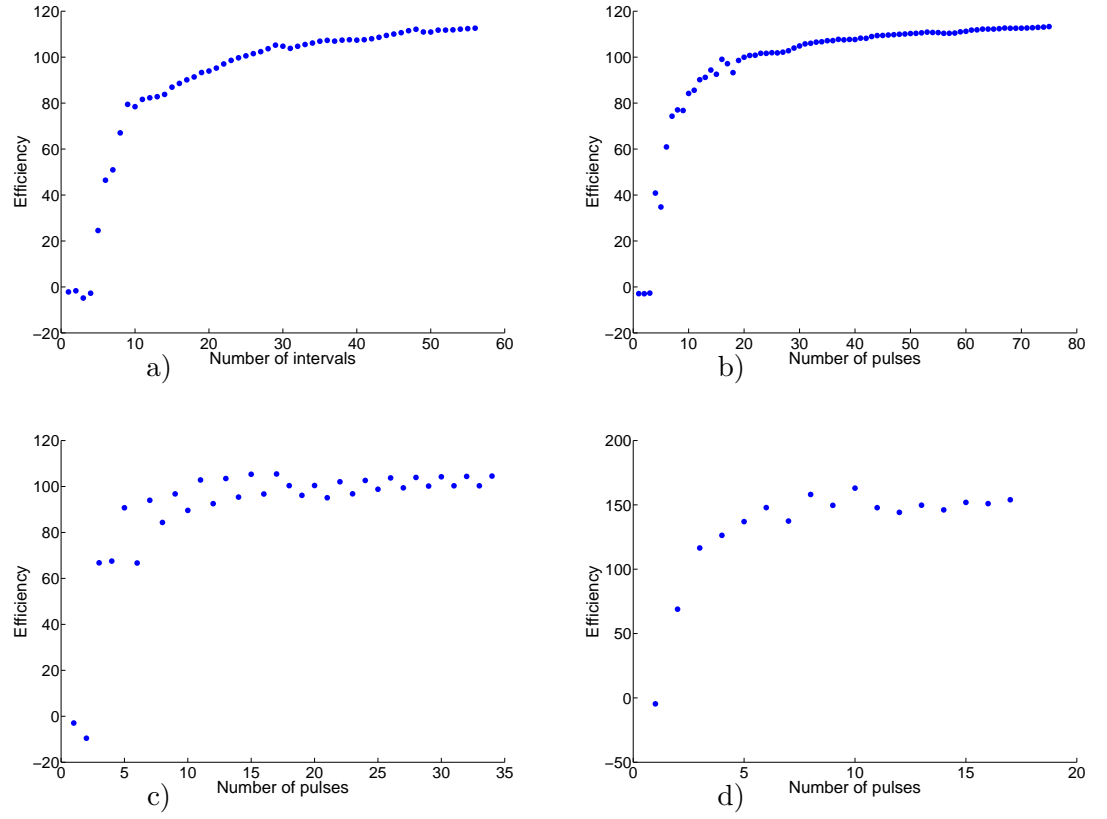


Figure 4.19: The drag reduction efficiency for: a) infinitely long filament b) $L/D = 4/3$ c) $L/D = 2$ d) $L/D = 4$

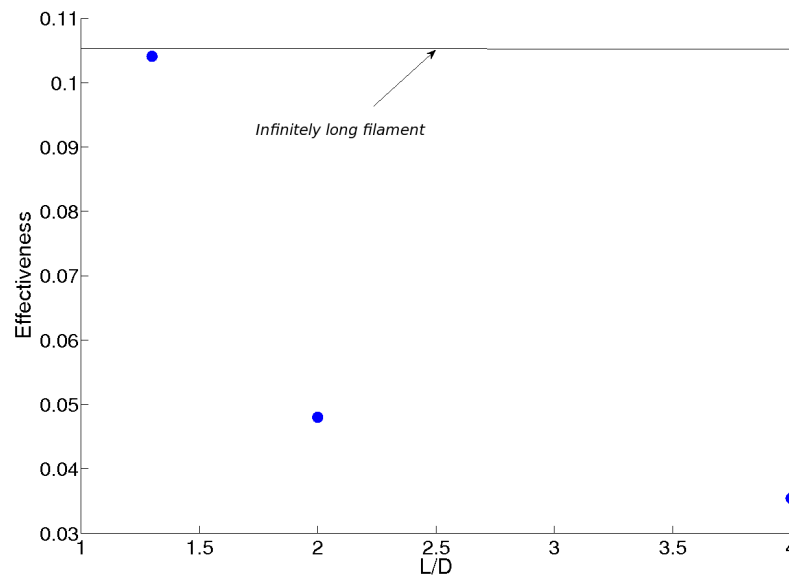


Figure 4.20: Asymptotic values for effectiveness

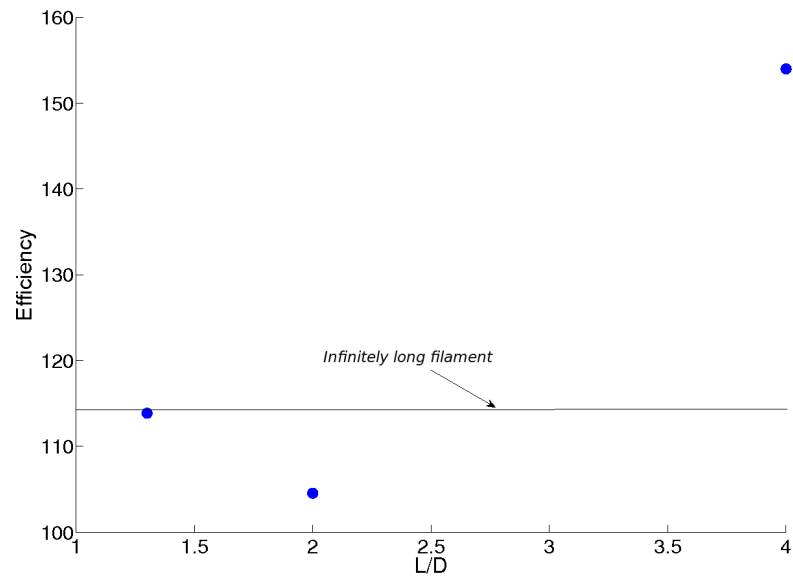


Figure 4.21: Asymptotic values for efficiency

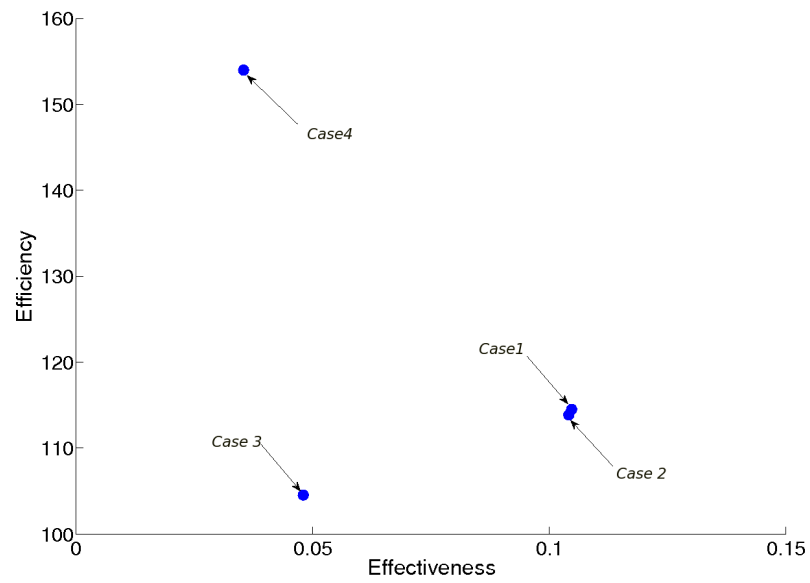


Figure 4.22: Drag reduction efficiency vurses effectiveness

Chapter 5

Conclusions - Future Work

Studying the interaction of an infinitely long filament and a train of finite filaments of different durations with the shock layer formed ahead of a blunt cylinder has demonstrated specific phenomena which can be further utilized to analyze the drag reduction over the blunt body using MW energy deposition. The basic phenomena explaining the flow structure are

1. Modification of the shape of the bow shock (lensing effect).
2. Generation of toroidal vortex region.
3. Formation of stagnation point and consequent aerodynamic streamlining of the body.
4. Convection of the vortex region past the cylinder (Cases 2–4).
5. Formation of weak shocks normal to the front surface of the body (Cases 1–3)
6. Formation of additional weak shocks within the shock layer.

Examining the efficiency of drag reduction for the cases of infinitely long filament as well as the train of finite filaments with the cylindrical shock layer has led to the result that MW energy deposition increases the efficiency of drag reduction dramatically. Also, computations show that the efficiency in drag reduction does not vary significantly when the filaments become finite (cases 1 and 2). This is an interesting result, since in practice, only finite MW pulses could be generated. Finally, there exists the pareto set of non-dominated configurations (cases 1, 2 and 4). The maximum efficiency in case 4 is due to the small amount of energy added to create the MW beam and the drag reduction effectiveness is minimum in this case. Furthermore, the maximum effectiveness is that of the infinitely long filament case which does not show the same result for the efficiency.

This work can be expanded by studying the interaction of an off-axis filament with the shock layer. In this case, the problem would not be axisymmetric anymore and a complete 3-D analysis is required. Furthermore, the heat transfer effect can come into consideration which requires viscous simulations.

Chapter 6

Numerical Schlieren

The flow images resulting from experiment are usually Schlieren pictures giving patterns integrated along the spanwise direction. To compare the numerical flowfields with experimental ones, usually an averaged density gradient field is calculated as

$$\overline{\nabla\rho}(x, y) = \frac{1}{L_z} \int |\nabla\rho(x, y, z)| dz \quad (6.1)$$

Then it is visualized using the “numerical Schlieren” technique put forward by [30] (as a half-tone grey-scale picture with a special nonlinear scale).

The procedure is as follows. First, the density gradient is computed in plane $z = 0$

$$\nabla\rho(x, y) = \sqrt{\left(\frac{\partial\rho}{\partial x}\right)^2 + \left(\frac{\partial\rho}{\partial y}\right)^2} \quad (6.2)$$

Next, a special non-linear scale for the above is determined. The following function is used here

$$Sch(x, y) = \exp(-c_k S(x, y)) \quad (6.3)$$

where

$$S(x, y) = \frac{|\nabla\rho(x, y)| - |\nabla\rho(x, y)|_o}{|\nabla\rho(x, y)|_1 - |\nabla\rho(x, y)|_o} \quad (6.4)$$

Here, $|\nabla\rho(x, y)|_o = c_o |\nabla\rho(x, y)|_{\max(x, y)}$, $|\nabla\rho(x, y)|_1 = c_1 |\nabla\rho(x, y)|_{\max(x, y)}$ and the constants are chosen as $c_o = -0.001$, $c_1 = -0.05$ and $c_k = -0.3$.

This function is then plotted in grey scale.

References

- [1] R.G. Adelgren, G.S. Elliott, D. Knight, A. Zheltovodov, and A. Beutner. Energy deposition in supersonic flow. In *AIAA Paper No. 2001-0885*, January 2001.
- [2] O. Azarova, V. Grudnitsky, and Y. Kolesnichenko. Numerical analysis of a thin low density channel effect on supersonic flow past bodies with wedge-shaped ledges. *Mathematical Modeling*, 18(5):104–112, 2005.
- [3] O. Azarova and Y. Kolesnichenko. On details of flow structure during the interaction of an infinite rarefied channel with cylindrical shock layer. In *Proceedings of the Seventh International Workshop on Magnetoplasma Aerodynamics*, Moscow, 2007. Institute of High Temperatures RAS.
- [4] O. Azarova and Y. Kolesnichenko. Numerical modeling of a thin low density channel effect on supersonic flow over cylinder body with complicated cavity. *Mathematical Modeling*, 20, 2008.
- [5] P. Bletzinger, B. Ganguly, D. VanWie, and A. Garscadden. Plasmas in high speed aerodynamics. *Journal of Physics*, 38:R33–R57, 2005.
- [6] V. Brovkin, S. Afanasev, D. Khmara, and Y. Kolesnichenko. Microwave discharge control by magnetic field. In *AIAA Paper No. 2004-0357*, January 2004.
- [7] V. Brovkin, S. Afanasev, D. Khmara, and Y. Kolesnichenko. Experimental investigation of combined laser–DC–MW discharges. In *AIAA Paper No. 2006-1459*, January 2006.
- [8] P.K. Chang. Separation of flows. Pergamon Press, 1970.
- [9] F. Farzan, D. Knight, O. Azarova, and Y. Kolesinichenko. Interaction of microwave filament and blunt body in supersonic flows. In *AIAA Paper No. 2008-1356*, January 2008.
- [10] P.Y. Georgievskii and V.A. Levin. Supersonic flow over bodies in the presence of external energy input. *Journal of Technical Physics*, 14(8):684–687, 1988.
- [11] S. K. Godunov. A difference scheme for numerical computation of discontinuous solution of hydrodynamic equations. *Math. Sbornik*, 1959. 47.
- [12] C. Hirsch. Numerical computation of internal and external flows. New York, 1997. John Wiley & Sons.
- [13] D. Knight. Elements of numerical methods for compressible flows. New York, 2006. Cambridge University Press.
- [14] D. Knight. Brief survey of high speed flow control using microwave energy deposition. In *EUCASS*, Brussels, Belgium, 2007.

- [15] D. Knight and Y. Kolesnichenko. A survey of aerodynamic flow control at high speed by microwave energy deposition. In *7th Workshop on Magneto-Plasma Aerodynamics*, Moscow, Russia, April 2007. Institute of High Temperature RAS.
- [16] D. Knight, V. Kuchinsky, A. Kurankov, and E. Sheikin. Survey of aerodynamic flow control at high speed using energy additon. In *AIAA Paper No. 2003-0525*, January 2003.
- [17] D. Knight, V. Kuchinsky, A. Kuranov, and E. Sheikin. Aerodynamic flow control at high speed using energy deposition. In *Fourth Workshop on Magneto-Plasma Aerodynamics*, Moscow, Russia, April 2002. Institute of High Temperatures RAS.
- [18] Y. Kolesnichenko, V. Brovkin, O. Azarova, D. Khmara, V. Lashkov, I. Mashek, and M. Ryvkin. Fine structure of MW discharge: evolution scenario. In *AIAA Paper No. 2003-0362*, January 2003.
- [19] Y. Kolesnichenko, V. Brovkin, S. Leonov, A. Krylov, V. Lashkov, I. Mashek, A. Gorynya, and M. Ryvkin. Investigation of AD-body interaction with microwave discharge region in supersonic flow. In *AIAA Paper No. 2001-0345*, 2001.
- [20] Y. Kolesnichenko, V.G. Brovkin, O. Azarova, and V.G. Grudnitsky. Microwave energy release regimes for drag reduction in supersonic flows. In *AIAA Paper No. 2002-0353*, pages 1–13, 2002.
- [21] V. Lashkov, I. Mashek, Y. Anisimov, V. Ivanov, Y. Kolesnichenko, and O. Azarova. Method of vortex flow intensification under MW filament interaction with shock layer on supersonic body. In *AIAA Paper No. 2006-0404*, January 2006.
- [22] V. Lashkov, I. Mashek, Y. Anisimov, V. Ivanov, Y. Kolesnichenko, M. Ryvkin, and A. Gorynya. Gas dynamic effect of microwave discharge on supersonic cone-shaped bodies. In *AIAA Paper No. 2004-0671*, January 2004.
- [23] V. Lashkov, I. Mashek, Y. Anisimov, and Y. Kolesnichenko. Influence of microwave discharge plasma on AD-body characteristics in supersonic flow. In *Third Workshop on Thermodynamical and Plasma Processes in Aerodynamics*, pages 260–270, Russia, July 2003.
- [24] B. Van Leer. Flux vector splitting for the Euler equations. In *Eighth International Conference on Numerical Methods in Fluid Dynamics*, volume 170, pages 507–512, Springer-Verlag, Berlin, 1982.
- [25] H. W. Liepmann and A. Roshko. Elements of gasdynamics. New York, 2001. Dover Publications.
- [26] A. MacDonald. Microwave breakdown in gases. New York, 1966. John Wiley & Sons.
- [27] I. Mashek, Y. Anisimov, V. Lashkov, Y. Kolesnichenko, V. Brovkin, and M. Ryvkin. Microwave discharge initiated by laser spark in air. In *AIAA Paper No. 2004-0358*, January 2004.
- [28] E. Meshkov. Instability of boundary between two gases accelerated by a shock wave. *Izv. AN SSSR, MGG*, 1969. No. 5, pp. 151-157.

- [29] S.S. Milichev, M.D. Pavlovich, S. Ristich, and A. Vitich. On the influence of spike shape at supersonic flow past blunt bodies. Series: Mechanics, Automatic Control and Robotics, 2002. N12.
- [30] J. Quirk. A contribution to the great Riemann solver debate. *Int J Numerical Methods in Fluids*, 1994. 18:555–574.
- [31] www.aerosft.com.
- [32] A. Zheltovodov. Development of studies on energy deposition for application to the problems of supersonic aerodynamics. Technical Report 10–2002, Khristianovich Institute of Thermodynamical and Applied Mechanics, Novosibirsk, Russia, 2002. Preprint.
- [33] A. Zheltovodov, E. Pimonov, and D. Knight. Energy deposition influence on supersonic flow over axisymmetric bodies. In *AIAA Paper No. 2007–1230*, January 2007.

Vita

Farnaz Farzan

Education

August 2005 BS in Mechanical Engineering, University of Tehran, Tehran, Iran, GPA:15/20.

July 2008 MS in Mechanical and Aerospace Engineering, Rutgers, The State University of New Jersey, New Brunswick, New Jersey, GPA:3.85/4.00.

Work Experience

Summer 2003 and 2004 Intern, Gorouh-e-Chahar Consulting Engineering, Piping and HVAC Department.

September 2004–January 2005 Teaching Assistant, Department of Mechanical Engineering, University of Tehran, Tehran, Iran.

September 2006–June 2008 Graduate Assistant, Department of Mechanical and Aerospace Engineering, Rutgers, The State University of New Jersey, New Brunswick, New Jersey.

Publications and Presentations

2008 Farzan, F., Knight, D., Azarova, O., Kolesinichenko, Y., Interaction of Microwave Filament and Blunt Body in Supersonic Flows, *AIAA Paper No. 2008-1356*, January.